Article

Proposing Optimized Random Forest Models for Predicting Compressive Strength of Geopolymer Composites

Feng Bin [1,2], Shahab Hosseini [3], Jie Chen [1], Pijush Samui [4], Hadi Fattahi [5] and Danial Jahed Armaghani [6,*]

1 School of Resources and Safety Engineering, Chongqing University, Chongqing 400044, China; binfeng@stu.cqu.edu.cn (F.B.); jiechen023@cqu.edu.cn (J.C.)
2 Feny Co., Ltd., Changsha 410083, China
3 Department of Mining Engineering, Faculty of Engineering, Tarbiat Modares University, Tehran 1411713116, Iran; h.seyyedshahab@modares.ac.ir
4 Department of Civil Engineering, National Institute of Technology, Patna 800005, India; pijush@nitp.ac.in
5 Faculty of Earth Sciences Engineering, Arak University of Technology, Arak 3818146763, Iran; h.fattahi@arakut.ac.ir
6 School of Civil and Environmental Engineering, University of Technology Sydney, Ultimo, NSW 2007, Australia
* Correspondence: danial.jahedarmaghani@uts.edu.au

Abstract: This paper explores advanced machine learning approaches to enhance the prediction accuracy of compressive strength (CoS) in geopolymer composites (GePC). Geopolymers, as sustainable alternatives to Ordinary Portland Cement (OPC), offer significant environmental benefits by utilizing industrial by-products such as fly ash and ground granulated blast furnace slag (GGBS). The accurate prediction of their compressive strength is crucial for optimizing their mix design and reducing experimental efforts. We present a comparative analysis of two hybrid models, Harris Hawks Optimization with Random Forest (HHO-RF) and Sine Cosine Algorithm with Random Forest (SCA-RF), against traditional regression methods and classical models like the Extreme Learning Machine (ELM), General Regression Neural Network (GRNN), and Radial Basis Function (RBF). Using a comprehensive dataset derived from various scientific publications, we focus on key input variables including the fine aggregate, GGBS, fly ash, sodium hydroxide (NaOH) molarity, and others. Our results indicate that the SCA-RF model achieved a superior performance with a root mean square error (RMSE) of 1.562 and a coefficient of determination (R^2) of 0.987, compared to the HHO-RF model, which obtained an RMSE of 1.742 and an R^2 of 0.982. Both hybrid models significantly outperformed traditional methods, demonstrating their higher accuracy and reliability in predicting the compressive strength of GePC. This research underscores the potential of hybrid machine learning models in advancing sustainable construction materials through precise predictive modeling, paving the way for more environmentally friendly and efficient construction practices.

Keywords: geopolymer composites; compressive strength; machine learning; Harris Hawks optimization; sine cosine algorithm; random forest

1. Introduction

The manufacturing procedures of Ordinary Portland Cement (OPC), which is the cementitious material that is extensively used in concrete all over the globe, are connected with a high energy demand and large CO_2 emissions. This is because of the fact that OPC is the cementitious material that is used in concrete [1–3]. The production of OPC is responsible for around 4 billion tons of carbon dioxide emissions each year, which accounts for approximately 5–7% of the total CO_2 emissions globally [4,5]. Many strategies have been implemented to try to lessen the impacts of OPC creation and usage due to growing environmental preservation problems and climate change implications [6–8]. To reduce the dependency on organic matter cement (OPC), the use of supplemental cementitious

materials (SCMs) and the recovery of materials that have not been utilized are both included in the aforementioned procedures [9–11]. Despite this, there are usually controls on the ratios of these SCMs substituted for OPC [12,13]. A good example of this would be fly ash, which, although displaying pozzolanic qualities throughout the different phases of OPC hydration, has only a marginal impact on the early stages of strength development [14–16]. Due to the fact that the incorporation of fly ash may slow down the pace of early hydration and extend the amount of time it takes for the material to set [17,18], its use in large quantities is restricted. In order to totally replace OPC, one of the most investigated methods is to use alkali activation to produce cementitious binders that are less harmful to the environment [19,20]. OPC clinker may be produced without the high-powered, elevated-temperature heating process [21,22]. Alkali-activated materials, also known as AAMs, do not need this approach. AAMs, which are sometimes referred to as geopolymers, are polymeric alum inosilicate cementing components that have three-dimensional spatial complex topologies. These ingredients are activated using an alkaline agent, such as sodium hydroxide or sodium silicate, and are mostly constituted of industrial wastes such as fly ash [23,24]. Geopolymers are characterized by their one-of-a-kind chemical makeup, which confers upon them exceptional mechanical performance and durability. The method's main binder component is the reuse of waste resources, making it more environmentally friendly than OPC-based mixtures [25,26].

In an attempt to achieve a reduction in the number of repeats that are not essential in experiments and the amount of ingredients that are wasted, predictive models for material strength are currently being created. Best-fit curves, which are generated based on regression analysis, are among the many popular models that are used in the process of simulating the characteristics of concrete. On the other hand, with cementitious materials being nonlinear in nature [27], regression approaches that are developed in this way would not adequately capture the fundamental behavior of the material. In addition, regression methods have the potential to inaccurately estimate the importance of certain components [28]. Artificial intelligence modeling approaches, such as controlled machine learning (ML), are some of the most advanced and well-established techniques used in contemporary research [29–35]. Fuzzy systems and fuzzy numbers have found acceptable applications in mining and civil engineering domains [36–38]. For the purpose of modeling responses, these approaches make use of input variables, and the yield models are backed by experimentation. In order to predict the features of concrete and bituminous mixes, machine learning approaches are used [39–42]. While most previous machine learning-based studies [43–45] concentrated on predicting the compressive strength (CoS) of substances using orthopedic polymer innovation, only a few studies focused on forecasting the characteristics of geopolymer mixture mixtures.

The use of machine learning techniques in civil and concrete engineering projects has also received a lot of attention. Mustapha et al. [46] evaluated gradient-boosting ensemble models for quaternary mix concrete compressive strength prediction in great detail. Their results show that CatBoost excels in predictive accuracy, achieving an R^2 value of 0.9838, showcasing notable enhancements compared to other gradient-boosting models. In a similar fashion, Alhakeem et al. [47] utilized a combination of a hybrid Gradient Boosting Regression Tree (GBRT) model and GridSearch CV hyperparameter optimization to forecast the compressive strength of environmentally friendly concrete. Grid search optimization significantly improved model performance, resulting in an R^2 of 0.9612 and an RMSE of 2.3214 for this hybrid model. Additionally, Faraz et al. [48] performed studies on the prediction of metakaolin concrete's compressive strength, utilizing Gene Expression Programming (GEP) and Multigene Expression Programming (MEP). The highest MEP model had a R^2 value of 0.96, demonstrating that MEP models outperformed GEP models. This research also found that the water–binder ratio, superplasticizer percentage, and age are crucial factors that affect compressive strength. Shah et al. [49] applied MEP to simulate the mechanical characteristics of concrete made from E-waste aggregates, obtaining excellent precision with R-values above 0.9 for forecasting both compressive and

tensile strength. The water–cement ratio and the percentages of E-waste aggregate were shown to be the most significant elements in the sensitivity study.

These studies show the potential of advanced machine learning models, such as ensemble and hybrid approaches, in predicting sustainable concrete properties accurately. They also emphasize the significance of optimizing parameters and conducting sensitivity analysis to improve model performance and comprehend the impacts of different input factors.

Dey et al. [50] saw promise in geopolymer concrete's ability to include waste elements such as MT and recovered glass powder (GP) as environmentally friendly alternatives. Their research utilized response surface methodology to determine the best material ratios for achieving the highest compressive strength. Thorough assessments were carried out on the fresh-state properties, mechanical traits, and long-term durability of concrete mixtures. The researchers discovered that GP enhances the ease of work whereas MT reduces it because of its higher fineness and larger surface area. Adding GP and MT was said to improve compressive strength by as much as 25% while the use of only GP may have slightly decreased mechanical properties. Both materials have a limited impact on flexural and splitting tensile strengths compared to compressive strength. GP and MT mixtures surpass standard benchmarks in durability tests, which include quick chloride permeability tests and 300 freeze–thaw cycles. The research found that combining GP and MT enhances durability and boosts mechanical properties, highlighting their potential as eco-friendly alternatives in making concrete. In a separate study, Martini et al. [51], to further the development of environmentally responsible building practices, investigated the mechanical properties of concrete mixes that included recycled concrete aggregate (RCA) from structures that had been destroyed in Abu Dhabi. With varying percentages of recycled aggregate (0%, 20%, 40%, 60%, and 100%), they used ground granulated blast furnace slag and fly ash as supplementary cement ingredients in seventy concrete mixtures. By conducting tests involving compression from one direction and bending, the researchers discovered that concrete containing 20% recycled concrete aggregate (RCA) had a strength of more than 45 MPa, making it suitable for use in structures.

The compressive strength of geopolymer concrete (CoSGePC) has been the subject of several efforts to be calculated in an environment that is monitored, which are also referred to as direct determination. Wakjira et al. [52] have introduced a fresh approach for predicting strength and conducting the multi-objective optimization (MOO) of ultra-high-performance concrete (UHPC) that is both economical and friendlier to the environment, enabling smart, sustainable, and resilient construction methods. Their structure combines a range of tree and boosting ensemble machine learning models in order to create a precise and trustworthy prediction system for the uniaxial compressive strength of UHPC. Their optimized models have been merged to create a super learner model, which acts as a strong predictive tool and one of the optimization objectives in the multi-objective optimization problem. T.G. Wakjira and M.S. Alam [53] developed a predictive model using interpretable machine learning (ML) to address challenges in the performance-oriented seismic design (PBSD) of ultra-high-performance concrete (UHPC) bridge columns. UHPC, valued for its exceptional strength, toughness, and durability, encounters a substantial challenge in accurately measuring damage levels with suitable engineering demand parameters (EDPs). The aforementioned authors' research attempts to close that divide by forecasting the drift ratio threshold conditions of UHPC bridge columns through four different stages of damage. Table 1 contains various literary models used to forecast different properties of concrete. Many other ML techniques employed to predict the properties of the CoSGePC besides some of these techniques are the Support Vector Machine (SVM), Gene Expression Programming (GEP), Artificial Neural Network (ANN), Decision Tree (DT), random forest (RF), Data Envelopment Analysis (DEA), Response Surface Methodology (RSM), Adaptive Neuro Fuzzy Inference System (ANFIS), Micali–Vazirani Algorithm (MV), Retina Key Scheduling Algorithm (RKSA), Gradient Boosting (GB), Gaussian Process Regression (GPR), Multivariate Adaptive Regression Splines (MARS), Support Vector Machine Regression

(SVMR), Nonlinear Regression (NLR), Multi-linear Regression (MLR), Linear Regression (LR), Pure Quadratic (PQ), Interaction (IA), and Complete Quadratic (FQ). These methods are highlighted in Table 1.

Table 1. Applying AI methods to anticipate different properties of concrete.

Author	Year	Technique	Number of Data
Huang et al. [54]	2021	SVM	114
Sarir et al. [55]	2019	GEP	303
Balf et al. [56]	2021	DEA	114
Ahmad et al. [57]	2021	GEP, ANN, DT	642
Azimi-Pour et al. [58]	2020	SVM	-
Saha et al. [59]	2020	SVM	115
Hahmansouri et al. [60]	2019	GEP	54
Aslam et al. [61]	2020	GEP	357
Farooq et al. [62]	2020	RF and GEP	357
Asteris and Kolovos [63]	2019	ANN	205
Selvaraj and Sivaraman [64]	2019	IREMSVM-FR with RSM	114
Zhang et al. [65]	2019	RF	131
Kaveh et al. [66]	2018	M5MARS	114
Sathyan et al. [67]	2018	RKSA	40
Vakhshouri and Nejadi [68]	2018	ANFIS	55
Belalia Douma et al. [69]	2017	ANN	114
Abu Yaman et al. [70]	2017	ANN	69
Ahmad et al. [71]	2021	GEP, DT, and Bagging	270
Farooq et al. [72]	2021	ANN, bagging and boosting	1030
Bušić et al. [73]	2020	MV	21
Javad et al. [74]	2020	GEP	277
Nematzadeh et al. [75]	2020	RSM, GEP	108
Güçlüer et al. [76]	2021	ANN, SVM, DT	100
Ahmad et al. [77]	2021	ANN, DT, GB	207
Asteris et al. [78]	2021	ANN, GPR, MARS	1030
Emad et al. [79]	2022	ANN, M5P,	306
Shen et al. [80]	2022	XGBoost, AdaBoost, and Bagging	372
Kuma et al. [81]	2022	GPR, SVMR	194
Jaf et al. [82]	2023	NLR, MLR, ANN	236
Mahmood et al. [83]	2023	NLR, M5P, ANN	280
Ali et al. [84]	2023	LR, MLR, NLR, PQ, IA, FQ	420

The significance of the research presented in this paper lies in its innovative approach to improving the prediction accuracy of compressive strength (CoS) in geopolymer composites (GePCs). Geopolymers are environmentally friendly alternatives to Ordinary Portland Cement (OPC), whose production is responsible for significant CO_2 emissions. The paper addresses the critical need for accurate predictive models to reduce experimental redundancies and resource waste in GPC development. Traditional regression models often fail to capture the nonlinear behaviors of cementitious materials and may inaccurately estimate the importance of certain components. By contrast, this research leverages advanced machine learning (ML) techniques, specifically supervised machine learning (SML) models, to enhance prediction accuracy. The researchers used data from various scientific publications, paying particular attention to important input variables including fly ash, fine aggregate, ground granulated blast furnace slag (GGBS), sodium hydroxide (NaOH) molarity, and other similar factors. They compared two hybrid models—the Harris Hawks Optimization with Random Forest (HHO-RF) and Sine Cosine Algorithm with Random Forest (SCA-RF) models—to traditional models. The results show that the hybrid models, especially the SCA-RF model, significantly improve prediction accuracy, as evidenced by performance metrics like the mean absolute error (MAE), root mean square error (RMSE), variance accounted for (VAF), and the coefficient of determination (R^2). This research provides valuable insights and methodologies for developing more efficient and accurate predictive models in the field of geopolymer composite materials, contributing to more sustainable construction practices.

2. Research Methodology

2.1. Harris Hawks Optimizer (HHO)

A machine learning tool called the HHO mimics the predator–prey dynamics of the Harris hawk, which include the elements of exploration, the process of transformation, and exploitation. The method needs less parameter tweaking and may perform global enquiries. As a result, it has a lot of mining capacity.

Search phase

Harris hawks are nocturnal hunters that use a combination of two methods to locate their prey:

$$X(t+1) \begin{cases} X_{rand}(t) - r_1|X_{rand}(t) - 2r_2X(t)|, & q \geqslant 0.5 \\ \left|X_{rabbit(t)} - X_m(t)\right| - r3[lb + r_4(ub - lb)], & q < 0.5 \end{cases} \tag{1}$$

Here, the subsequent repetition's value is $X(t)$ and the place in which the current iteration occurs is $X(t+1)$. There are currently t iterations. The prey site is X_{rabbit} (t), or a particular place with the highest level of wellness, and the selected independent participant is X_{rand} (t). The integers r_1, r_2, r_3, r_4, and q are randomly selected in [0, 1]. The strategy to be utilized is chosen at random using q. The equation for the average location of people in general, denoted as X_m (t), is demonstrated by Equation (2).

$$X_m(t) = \sum_{k=1}^{N} X_k(t)/N \tag{2}$$

The symbol X_k (t) represents the k-th person in the groups. The group's size is N.

The progression of growth and search

When the prey leaves, HHO alternates between searching and other development activities. Equation (3) explains escape power.

$$E = 2E_0\left(1 - \frac{t}{T}\right) \tag{3}$$

Here, T is the greatest number of repeats, E_0 is the random value in $[-1,1]$, and t is the number of repetitions. $|E| < 1$ enters the development phase whereas $|E| \geq 1$ enters the analysis stage (see Figure 1).

Phase of growth

This phase selects several growth methods by using r, a random number in [0, 1] (Figure 2).

As Equation (4) shows, it updates the location using the gentle siege technique whenever $0.5 \leq |E| < 1$ and $r \geq 0.5$.

$$X(t+1) = X_{rabbit}(t) - E|\Delta X(t)| \tag{4}$$

As described in Equations (5)–(7), the phase adjusts the location using the soft enveloping technique of asymptotic rapid subduction when $0.5 \leq |E| < 1$ and $r < 0.5$.

$$X(t+1) = \begin{cases} Y, & f(Y) < f(X(t)) \\ Z, & f(Z) < f(X(t)) \end{cases} \tag{5}$$

$$Y = X_{rabbit}(t) - E|JX_{rabbit}(t) - X(t)| \tag{6}$$

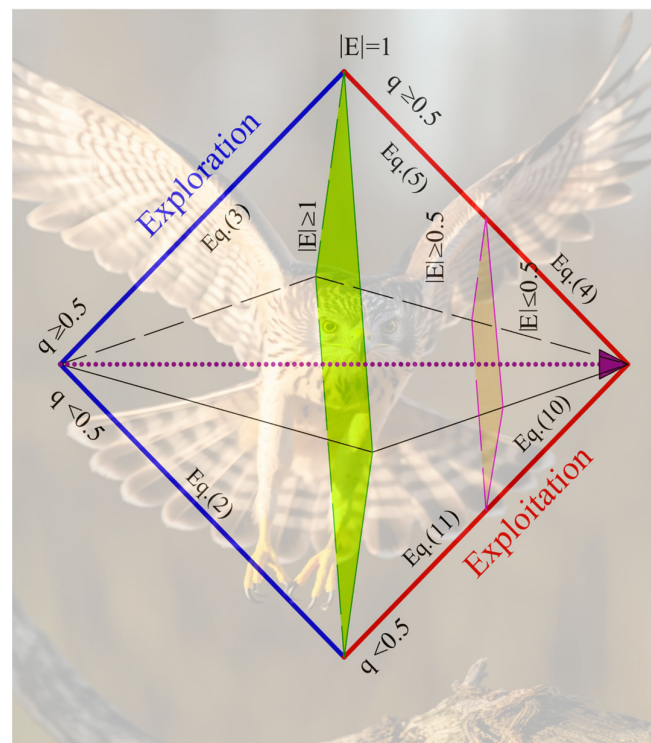$$Z = Y + S(Dim) \times Levy(Dim) \tag{7}$$

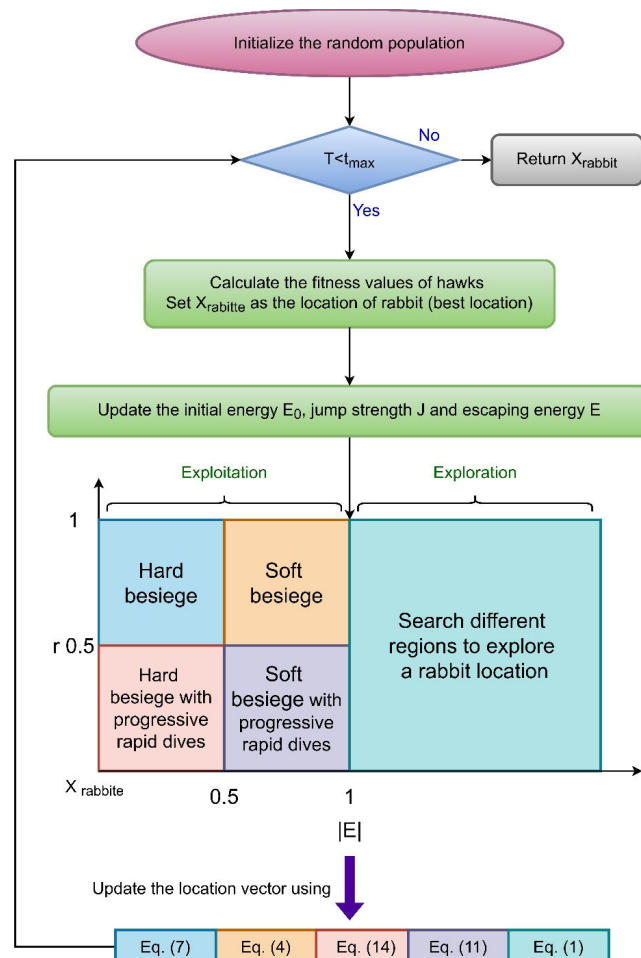**Figure 1.** Various phases in HHO algorithm.

Figure 2. Flowchart of HHO algorithm.

Here, Levy is Levi's flight, *Dim* is the issue dimension, *S* is the random vector *f()* of the *Dim* dimension, and the components within are random values in the range of [0, 1].

As indicated by Equations (8)–(10) for updating the location, the phase uses the complex enveloping method of asymptotic rapid descent when $|E| < 0.5$ and $|E| < 0.5$.

$$X(t+1) = \begin{cases} Y, & f(Y) < f(X(t)) \\ Z, & f(Z) < f(X(t)) \end{cases} \tag{8}$$

$$Y = X_{rabbit}(t) - E|JX_{rabbit}(t) - X_m(t)| \tag{9}$$

$$Z = Y + S(Dim) \times Levy(Dim) \tag{10}$$

The pseudo-code for HHO in Algorithm 1 is provided. HHO may change its developing habit from discovery to production depending on the escape power of the prey. During the flight behavior, the prey's power is drastically decreased.

Algorithm 1. Pseudo-code of HHO

1　　**Initialize the parameters** *popsize, MaxFes*
2　　**Initialize** a set of search agents *(solutions) (X)*
3　　While*(t ≤ MaxFes)*
4　　**Calculate** each of the search hawks by the objective function;
5　　**Update** X_{rabbit}(best loaction) and *best fitness*
6　　**For** i = 1 to *popsize*
7　　**Update** the *E* by **Equation (3)**;
8　　**Update** the *J*;
9　　**If** ($|E| \geq 1$).
10　**Update** the position of search agents using **Equation (1)**
11　**End If**.
12　**If** ($|E| < 1$).
13　**If** ($0.5 \leq |E| < 1$ and r ≥ 0.5).
14　**Update** the position of search agents using **Equation (4)**;
15　**End If**.
16　**If** ($|E| < 0.5$ and r ≥ 0.5).
17　**Update** the position of search agents using **Equation (5)**;
18　**End If**.
19　**If** ($0.5 \leq |E| < 1$ and r < 0.5).
20　**Update** the position of search agents using **Equations (6)–(8)**;
21　**End If**.
22　**If** ($|E| < 0.5$ and r < 0.5).
23　**Update** the position of search agents using **Equations (9)–(11)**;
24　**End If**.
25　**End If**.
26　**End For**.
27　**End While**.
28　**Return** X_{rabbit} and *best fitness*.

Strengthened hierarchies

HHO mimics different hawk behaviors during the hunting phase but does not represent other cognitive behaviors. Many animals and other species in nature exhibit certain social behaviors and hierarchies. To reinforce the individual relationships within the HHO population size, we thus implemented a hierarchy. This allows people with high levels of fitness to take the lead and guide the whole population to adjust their places appropriately. We initially rate everyone's fitness (fitness), and we designate *A*, *B*, and *C* as the three people who are the most fit, accordingly. These people receive updates individually.

Participant *A*'s position adjustment formula is expressed in Equation (11). By assessing the percentage of the staying duration of the method to the overall running periods with the Cauchy unpredictability amount, it is evident that the current location can move towards the ideal location. As the substitute's probability increases, the likelihood of this happening becomes less significant. This ensures that the method can prevent getting stuck in local optimization.

$$X^j(t+1) = \begin{cases} X^j_{rabbit(t)} & (\tan(pi \times (rand - 0.5)) < (1 - t/MaxFEs)) \\ X^j_{rabbit(t)} + G \times \left(X^j_m(t) - X^j_n(t) \right) & other \end{cases} \tag{11}$$

In this case, the character *j* denotes a certain dimension. The amount of the *j*-th category for every member *A*'s subsequent iteration is indicated by the formula $X^j(t+1)$. At the same time, the *j*-th measure of the optimal position for the *t*-th loop is represented by the equation $X^j_{rabbit}(t)$.

X^j_m and X^j_n represent an arbitrary choice of two people from the sample, with the condition that *m* and *n* are not the same, and neither is person *A*. The variable rand represents an integer with a probability in the range of [0, 1]. The variable *t* represents the current count of repetitions while MaxFEs represents the most significant number of repetitions. The quantity of *G* is determined by Equation (12).

$$G = \left(4 - t \times \left(\frac{4}{MaxFes} \right) \right) \times rand \tag{12}$$

The location refresh equation for person *B* is represented by Equation (13).

$$X^j(t+1) = \begin{cases} X^j(t) & rand > 0.5 \\ \left(X^k_A(t) + X^k_B(t) \right)/2 & other \end{cases} \tag{13}$$

The value of subcategory *j* for the individual *B* after the next repetition is represented by the parameter $X^j(t+1)$. For individual *B*, the quantity in the current cycle of dimensions, *j*, is represented by $X^j(t)$. The value of *k* defines the unsupervised selection of an aspect from the available ones. $X^k_A(t)$ represents the adoration of size *j* for individual *A*'s present reiteration whereas $X^k_B(t)$ represents the admiration of size *j* for person *B*'s contemporary repetition.

Lastly, we have person *C*, and their location update algorithm appears in Equation (14).

$$X^j(t+1) = \begin{cases} \left(X^j_Q(t) + X^j_R(t) \right)/2 & rand > 0.5 \\ \left(X^k_A(t) + X^k_B(t) + X^k_C(t) \right)/3 & other \end{cases} \tag{14}$$

In this case, $X^j(t+1)$ represents the outcome of each person's j dimensions' following iteration *C*. *Q* and *R* stand for the two individuals chosen at random from the pool of people and $X^j_Q(t)$ and $X^j_R(t)$ stand in for the j-scale values for the randomly chosen individuals in this rendition. Similarly, $X^k_A(t)$ represents the *j* dimension value for person *A*'s current repeat. The value of the *j* size for individual *B*'s current iteration is indicated by the notation $X^k_B(t)$. The current iteration of person C's j size is denoted by the notation. $X^k_C(t)$.

We have assigned three exceptional people to oversee local growth while others are responsible for carrying out the original refreshing of HHO. Simultaneously, we provide the most favorable location for the person *A* using a diminishing function. The method's substitution frequency diminishes as it progresses, allowing for local growth inside the examined area. Both persons *B* and *C* have a connection to individual *A*, which might enhance the communication among exceptional individuals. The updating technique of these three remarkable people is more accessible than that of the initial HHO. But EHHO has a higher speed than HHO. Our algorithm enhancement aims to enhance the resolution rate and precision, as well as the runtime efficiency and accuracy in feature selection duties, despite expanding computational difficulty.

2.2. Sine Cosine Algorithm (SCA)

In 2016, Mirjalili presented the SCA, a population-level optimization technique [85]. The basic principle behind SCA is that by utilizing Equations (15) and (16), every answer will adjust its location to the location of the most effective answer in the search area.

$$X_i^{k+1} = X_i^k + r_1 \times sin(r_2) \times \left| r_3 P_i^k - X_i^k \right| \tag{15}$$

$$X_i^{k+1} = X_i^k + r_1 \times cos(r_2) \times \left| r_3 P_i^k - X_i^k \right| \tag{16}$$

Hence, at iteration k, X_i^k denotes that particular solution's location in the *i*-th vector. The *i*-th degree of the greatest answer found so far is represented by P_i^k, the three random factors are r_1, r_2, and r_3, and the final value is indicated by Equations (15) and (16), which have been merged for their last update (see Figure 3), as is apparent in Equation (17), to streamline the formulas.

$$X_i^{k+1} = \begin{cases} X_i^k + r_1 \times sin(r_2) \times \left| r_3 P_i^k - X_i^k \right| & , r_4 < 0.5 \\ X_i^k + r_1 \times cos(r_2) \times \left| r_3 P_i^k - X_i^k \right| & , r_4 \geq 0.5 \end{cases} \tag{17}$$
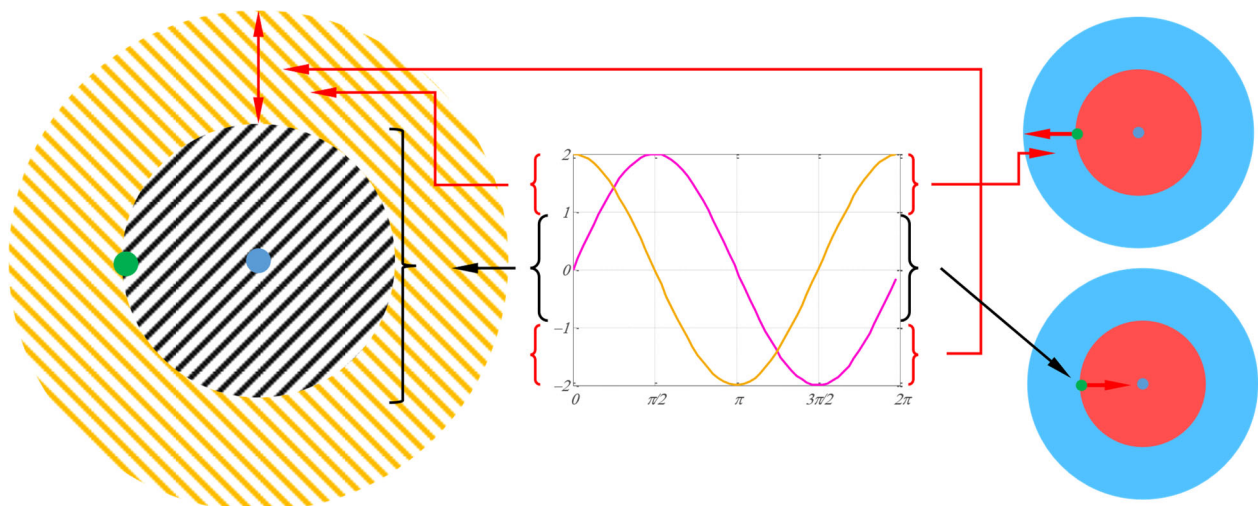
Figure 3. The method of updating an answer towards or away from the optimal option.

The goal of any metaheuristic technique should be to balance the processes of exploration and exploitation properly. Equation (18) illustrates how SCA achieves the equilibrium between discovery and extraction via optimization by reducing the region of sines and cosines.

$$r_1 = a - k\frac{a}{K} \tag{18}$$

Here, the factors K and K are the most significant number of and the number of current repetitions, respectively. A is a fixed value. Figure 4 shows how to reduce the sine and cosine area with repetitions at $a = 3$. The SCA method's pseudo-code is shown in Algorithm 2.

Algorithm 2. Pseudo-code of SCA.

Random initialization of population of search agents (solutions) (X)
Solution evaluation by the objective function
P = the optimal solution found so far.
while ($k < K$) **do**
    Update r_1, r_2, r_3 and r_4
    for each search agent in the population **do**
        if ($r_4 < 0.5$) **then**
            | $X_i^{k+1} = X_i^k + r_1 \times \sin(r_2) \times \left| r_3 P_i^k - X_i^k \right|$
        else if ($r_4 \geq 0.5$) **then**
            $X_i^{k+1} = X_i^k + r_1 \times \cos(r_2) \times \left| r_3 P_i^k - X_i^k \right|$
    Estimate the value of objective function for each search agent.
    Update P
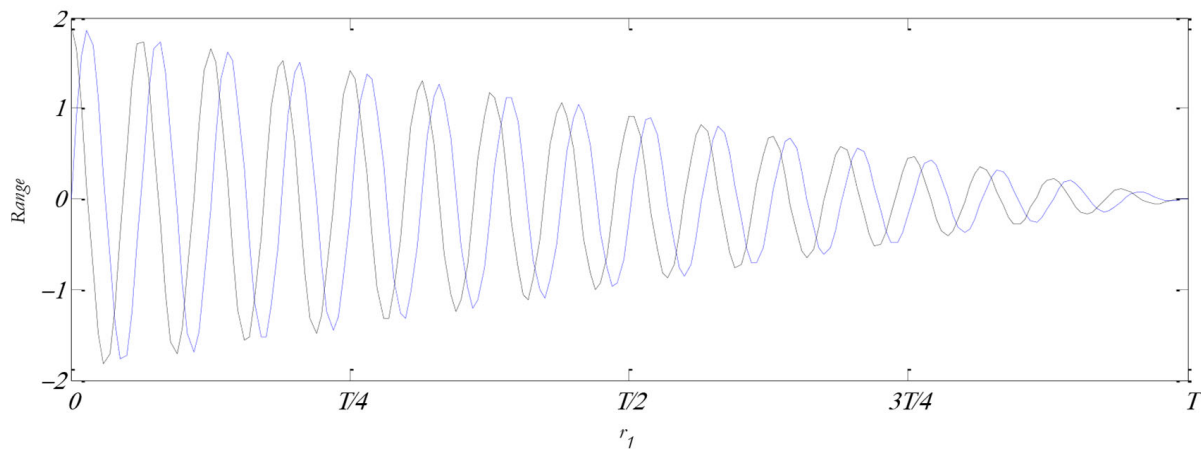   k = k + 1.
return P

Figure 4. The sine and cosine declining patterns.

2.3. Random Forest (RF) Algorithm

Ensemble learning techniques include the random forest algorithm. When dealing with data that have a lot of dimensions, it works well. In order to reduce the risk of model overfitting and increase overall accuracy, it builds many decision trees during training and then merges their classification outputs [86]. For the purpose of generating new training datasets, the random forest model uses a combination of random sampling and replacement. This method of random sampling reduces the impact of individual samples while increasing the model's variety and resilience. The decision trees are constructed using the random forest model using a feature-random-selection approach. In order to choose candidates, split attributes at each decision tree node, a subset of the whole feature set is randomly selected. (see Figure 5). The model's capacity to generalize is enhanced by reducing feature correlation via feature random selection. Last but not least, the random forest model uses voting to decide on classifications. Each decision tree makes a forecast for a classification job and the ultimate outcome is decided by a majority vote. The vote result may be written as follows, assuming the collection of classes is $\{c_1, c_2, \ldots, c_N\}$, and $h_i^j(x)$ represents the result of prediction of the decision tree h_i for class c_i.

$$H(x) = \begin{cases} c_j, & \sum\limits_{i=1}^{T} h_i^j(x) > 0.5 & \sum\limits_{k=1}^{N}\sum\limits_{i=1}^{T} h_i^k(x) \\ reject, & others \end{cases} \qquad (19)$$
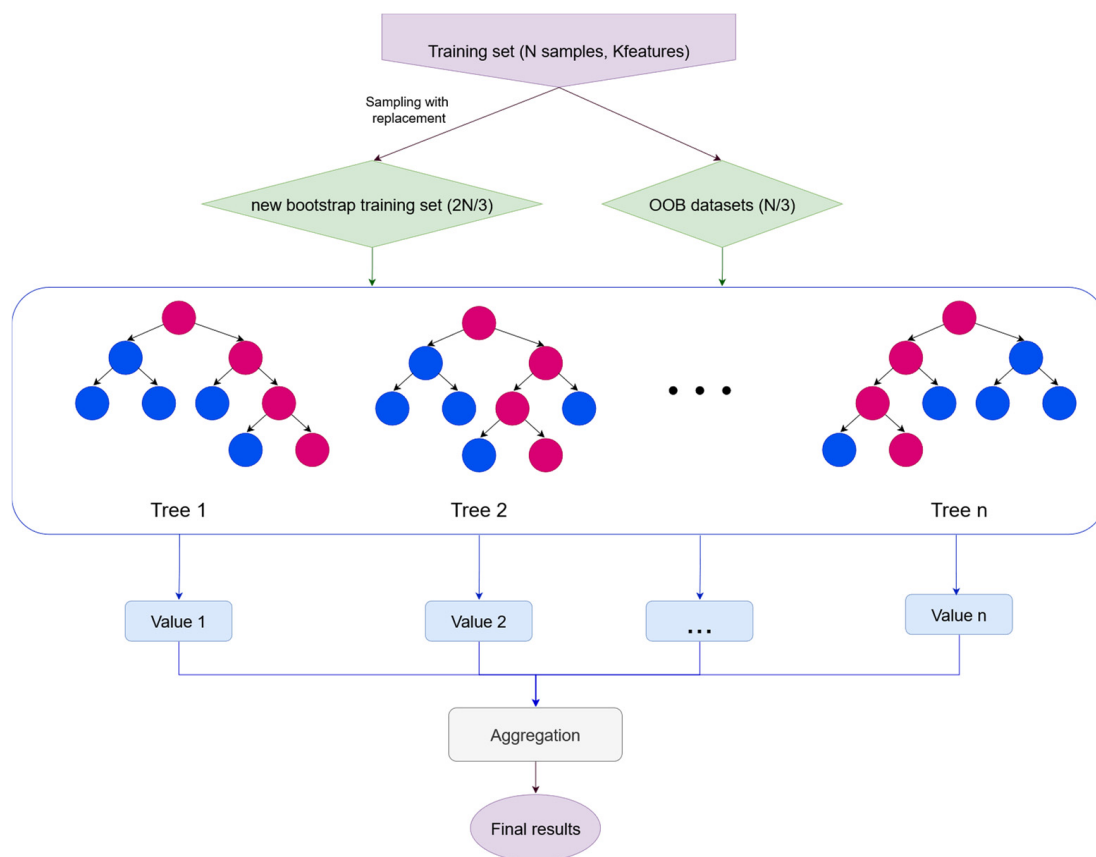
Figure 5. Architecture of RF algorithm.

3. Data Presentation

Supervised machine learning (SML) methods necessitate an assortment of input factors to achieve the desired predictive outcomes [87]. Information on geopolymer composites' compressive strength (CoS) values was derived from a number of scholarly articles in this study [88–126] (see Supplementary Materials). A random selection of experimental data was made from the existing literature to guarantee objectivity. Unlike many studies that focused on various properties of GePC, this research specifically collected data points related to CoS to facilitate the execution of the algorithms. The input variables for the algorithms included the fine aggregate, ground granulated blast furnace slag (GGBS), fly ash, sodium hydroxide (NaOH) molarity, NaOH quantity, water-to-solids ratio, sodium silicate (Na_2SiO_3), and gravel sizes of 10/20 mm and 4/10 mm, with CoS serving as the target output parameter. The performance of SML models is significantly influenced by the number and variety of input variables and datasets utilized. For this study, a total of 371 data points were compiled and used to run the machine learning algorithms, as detailed in the Supplementary Materials. These data points were selected based on mix proportions and the desired outcome, ensuring that each model had a consistent number of input parameters to generate the required outputs. Since the data were extracted from the existing literature, the experiments reflected variations in geographical locations, testing setups, and sample geometries. However, these differences did not impact the primary conclusions of the study as the models focused solely on input variables and their corresponding outcomes independent of the specific testing conditions. The descriptive statistics for each input variable are presented in Table 2. The data underwent a normalization process, which is a standard technique in data management. Normalization involves organizing data in a database to minimize redundancy and dependency issues, thereby enhancing the database's flexibility and integrity. Descriptive statistics encompass a range of measures that provide concise summaries of data, whether representing an entire population or a

subset. The mean, the median, and the mode are examples of measures that show core patterns. On the other hand, the maximum, the minimum, and the standard deviation highlight the variability that exists within the data.

Table 2. Properties of CoSGePC parameters.

Parameter	Abbreviation	Unit	Mean	Median	Standard Deviation	Kurtosis	Skewness	Min	Maximum
Fly ash	FA	kg/m^3	174.276	150.000	172.767	-1.554	0.252	0.000	523.000
Ground granulated blast furnace slag	GGBS	kg/m^3	213.449	233.000	162.307	-1.603	-0.013	0.000	450.000
Na_2SiO_3	Na_2SiO_3	kg/m^3	102.224	99.500	41.653	6.873	1.596	18.000	342.000
NaOH	NaOH	kg/m^3	59.994	64.000	30.566	-0.102	0.277	6.300	147.000
Fine aggregate	FAg	kg/m^3	732.746	723.500	138.443	5.537	1.435	459.000	1360.000
Gravel 4/10 mm	Gravel 4/10	kg/m^3	332.472	307.500	372.807	0.470	1.137	0.000	1257.000
Gravel 10/20 mm	Gravel 10/20	kg/m^3	742.391	816.500	363.549	0.117	-0.977	0.000	1298.000
Water/solids ratio	WS	-	0.332	0.330	0.095	0.278	0.410	0.120	0.630
NaOH Molarity	NaOH Molarity	-	8.103	9.600	4.569	-1.150	-0.018	1.000	20.000
Compressive strength of geopolymer concrete	CoSGePC	MPa	44.691	43.000	18.012	-0.783	0.303	10.000	86.080

When it comes to the input variables to the model, Table 2 has all the statistical jargon you could want. Figure 6 illustrates the violin plot of each input factor relative to the compressive strength. The diagonal plots show the frequency distribution while the off-diagonal representation shows the correlations between the input parameters and the output parameter. A comparable connection with the y-axis input/output parameter is shown by a trend in the line graph that is either positive or negative for each of the input/output parameters on the x-axis. In contrast, a straight line indicates no correlation between the parameters. Figure 7 further demonstrates the correlation patterns between the input parameters and the compressive strength values [127]. The graphical representation helps one visualize the nature and strength of these relationships, providing insight into how different input variables influence the output parameter, compressive strength, in the context of geopolymer composites. A summary of the dataset for anticipating the CoSGePC is listed in Table 3. Table 3 of the paper provides a summary of the dataset used in our study. The input variables include the fine aggregate (FA), ground granulated blast furnace slag (GGBS), sodium silicate (Na_2SiO_3), sodium hydroxide (NaOH), water-to-solids ratio (WS), and gravel sizes (4/10 mm, 10/20 mm), among others. The output variable is the compressive strength of geopolymer composites (CoSGePC). This dataset was sourced from multiple studies (as referenced) and serves as the basis for training our machine learning models.

Table 3. Summary of dataset for predicting CoSGePC.

Inputs									Output	
FA	GGBS	Na_2SiO_3	NaOH	FAg	Gravel 4/10	Gravel 10/20	WS	NaOH Molarity	CoSGePC	DOI
391	0	92	75	721	450	661	0.35	10	22	https://doi.org/10.1016/j.conbuildmat.2017.04.036 (accessed on 30 August 2017)
350	150	120	80	628	693	314	0.21	14	66	https://doi.org/10.1016/j.jobe.2018.09.010 (accessed on 1 November 2018)
360	40	107	53	644	399	798	0.21	10	23	https://doi.org/10.1016/j.conbuildmat.2018.04.008 (accessed on 30 May 2018)
280.24	190.95	113.87	75.91	828.12	0	809.58	0.23	14	80	https://doi.org/10.1016/j.conbuildmat.2018.04.016 (accessed on 10 June 2018)

Table 3. *Cont.*

|	Inputs								Output	
FA	GGBS	Na$_2$SiO$_3$	NaOH	FAg	Gravel 4/10	Gravel 10/20	WS	NaOH Molarity	CoSGePC	DOI
320	80	158.37	28.55	972.72	0	704.39	0.48	2.98	44.6	https://doi.org/10.1061/(ASCE)MT.1943-5533.0001618 (accessed on 12 December 2016)
360	40	114.3	45.7	651	446.4	762.6	0.21	14	40	https://doi.org/10.1016/j.matdes.2014.05.001 (accessed on 1 October 2014)
293	88	71.67	143.33	760	1005	0	0.36	6	37	https://doi.org/10.1016/j.conbuildmat.2013.05.107 (accessed on 1 October 2013)
400	0	114.3	45.7	651	1209	0	0.21	14	25	https://doi.org/10.1016/j.conbuildmat.2014.05.080 (accessed on 15 September 2014)
400	0	129.43	10.57	651	1209	0	0.22	12.67	27.7	https://doi.org/10.33915/etd.165 (accessed on 2013)
523	0	118	118	459	1124	0	0.26	10	36	https://doi.org/10.1155/2018/2460403 (accessed on 15 April 2018)
0	320	89.56	38.438	708.5	415.7	831.3	0.42	16	46.5	https://doi.org/10.14445/22315381/IJETT-V50P225 (accessed on 2017)
417	0	293	66	698	308	619	0.37	15	47	https://doi.org/10.1016/j.conbuildmat.2018.12.168 (accessed on 10 March 2019)
400	0	113	45	554	431	862	0.2	14	45	https://doi.org/10.1016/j.conbuildmat.2015.08.009 (accessed on 15 November 2015)
416	0	292	65	699	309	618	0.37	15	48.7	https://doi.org/10.1016/j.conbuildmat.2016.07.121 (accessed on 15 October 2016)
388	0	113	45	554	431	862	0.2	14	37.5	https://doi.org/10.1016/j.dib.2015.10.029 (accessed on 1 December 2015)
360	90	26.67	18.32	1247	415	0	0.16	2.42	64.5	https://doi.org/10.3389/fmats.2019.00009 (accessed on 14 February 2019)
225	225	112.5	45	627	0	1164	0.27	14	44.1	https://doi.org/10.1061/(ASCE)MT.1943-5533.0002333 (accessed on 1 July 2018)
90	360	81	22.77	1360	340	0	0.45	3.42	43	http://www.diva-portal.org/smash/record.jsf?pid=diva2:1098704 (accessed on 2017)
0	370	22.6	14.8	643	0	1217	0.43	2.39	36.2	https://doi.org/10.5281/zenodo.1093468 (accessed on 1 June 2014)
0	450	81.45	22.77	1332	331	0	0.45	3.42	50	https://doi.org/10.1155/2019/6903725 (accessed on 28 April 2019)
360	40	114.3	45.7	650	0	1210	0.29	14	21	https://dx.doi.org/10.3390/ma12050740 (accessed on 4 March 2019)
0	419	53	56	784	346	693	0.29	10	32.9	https://researchrepository.rmit.edu.au/permalink/61RMIT_INST/1lek7c1/alma9921861379101341 (accessed on 2009)
350	0	75.3	75.3	570	0	680	0.28	12	21.09	https://doi.org/10.1016/j.serj.2017.03.005 (accessed on 1 May 2017)
0	357	80.03	14.97	563	548	728	0.29	10	64	https://doi.org/10.1016/j.cemconcomp.2017.10.003 (accessed on 1 January 2018)
0	400	101.82	58.18	894	894	0	0.28	10	44.92	https://doi.org/10.1016/j.conbuildmat.2018.11.086 (accessed on 10 February 2019)
0	300	72	48	917	0	1090	0.25	1	16.69	https://doi.org/10.1061/(asce)mt.1943-5533.0002296 (accessed on June 2018)
467	0	234	147	784	346	693	0.22	10	22.37	https://researchrepository.rmit.edu.au/permalink/61RMIT_INST/13r5bm8/alma9921864291801341 (accessed on 2014)
400	0	96	64	651	446.4	726.6	0.21	14	12.62	https://doi.org/10.1063/1.5003513 (accessed on 29 September 2017)
360	40	114.3	45.7	651	446.4	726.6	0.2	14	40	https://doi.org/10.1016/j.matdes.2014.05.001 (accessed on 1 October 2014)
85	340	131.55	25.5	700.54	210.16	840.65	0.38	5	81.1	https://www.concrete.org/publications/internationalconcreteabstractsportal.aspx?m=details&i=51701073 (accessed on 8 January 2017)
349.2	38.8	138.7	19.96	620.8	0	1221.1	0.44	7.5	55.7	https://www.unsworks.unsw.edu.au/permalink/f/5gm2j3/unsworks_49397 (accessed on 2018)
0	300	18	12	822	247	986	0.44	2.39	39.54	https://doi.org/10.1016/j.jclepro.2019.01.332 (accessed on 1 May 2019)
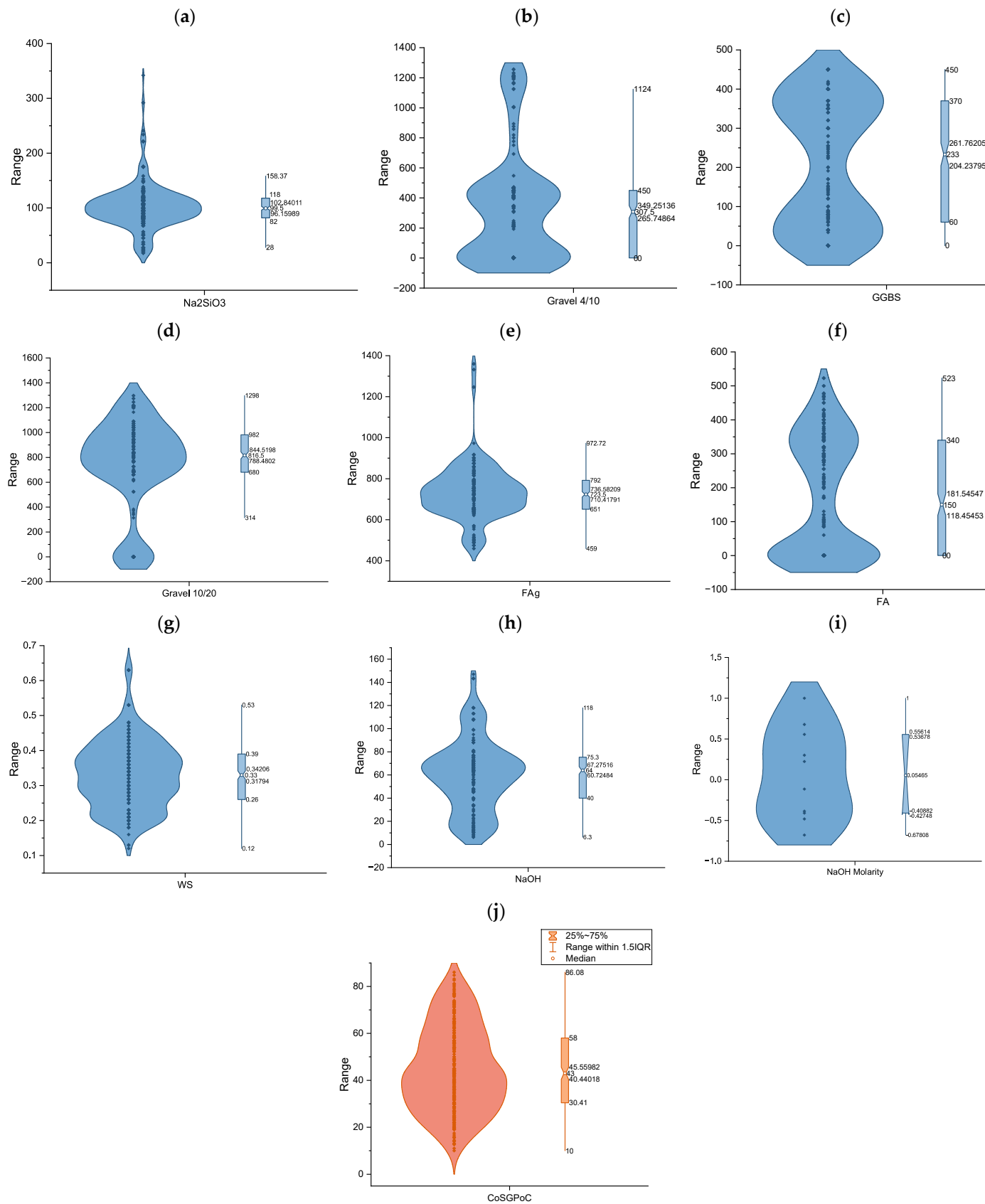
Figure 6. Violin plot of CoSGePC parameters: (**a**) Ni2SiO3, (**b**) Gravel 4/10, (**c**) GGBS, (**d**) Gravel 10/20, (**e**) FAg, (**f**) FA, (**g**) WS, (**h**) NaOH, (**i**) NaOH molarity, and (**j**) CoSGePC.
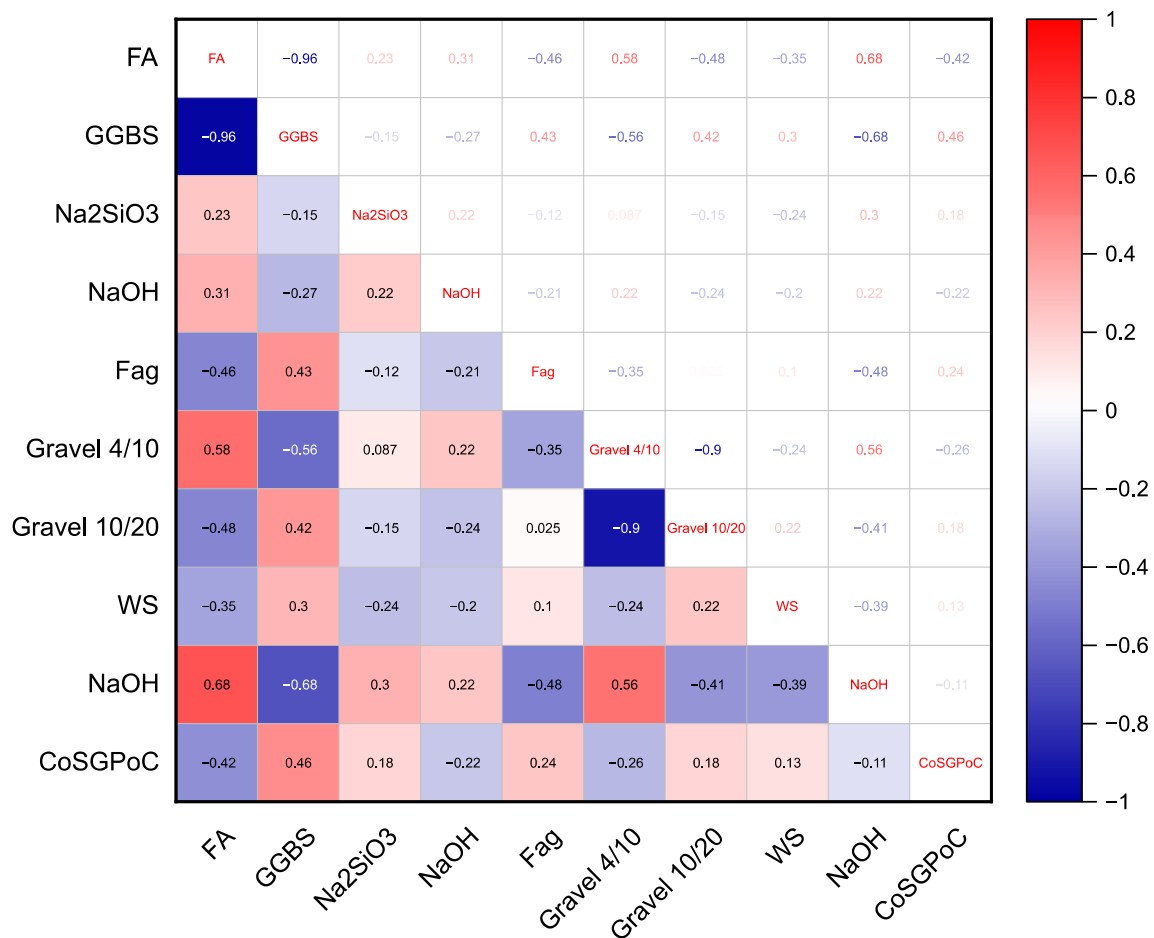
Figure 7. Heatmap of CoSGePC parameters.

4. Evaluations and Verifications of the Models

The process of constructing an intelligent model involves the verification and assessment of the performance of the model. For this reason, the researchers decided to use four different assessment indices. VAF, MAE, RMSE, and R^2 are the variables that measure the accuracy of the data with respect to the variables under consideration and are all significant measures of statistical significance. There are explanations of these indices that may be found in the published research [128].

Through the process of averaging the magnitude of the absolute error, the MAE is able to directly represent the inaccuracy in the forecast. In the event that the MAE value is low, it indicates that the projected CoSGePC is an excellent match for the actual CoSGePC. It is possible to acquire the expression of MAE as follows:

$$\text{MAE} = \frac{1}{n}\sum_{i=1}^{n}\left|CoSGPoC_i - CoS\hat{G}PoC_i\right| \tag{20}$$

The term "Root Mean Square Error" (RMSE) is an abbreviation that stands for "Root Mean Square Error," as the actual and projected CoSGePC are compared and the standard deviation of the regression error is computed. It has a high degree of responsiveness to the error, which magnifies the effect that it has on the final result. The root means square error, often known as the RMSE, is a mathematical statistic that represents the average variance between the values that were anticipated and those that are actually observed [129]. The calculation for it involves calculating the square root of the average of the squared disparities that exist between the values that were anticipated and those that have been discovered.

$$\text{RMSE} = \sqrt{\frac{1}{n}\sum_{i=1}^{n}\left(Co S\hat{G}PoC_i - CoSGPoC_i\right)^2} \tag{21}$$

A description of the performance of the prediction is provided by the VAF, which is provided in order to offer this description. For the purpose of accomplishing this objective, a comparison is made between the standard deviation of the fitting error and the standard deviation of the real CoSGePC. The use of it is not feasible if all of the values that are noticed are identical to one another. Specifically, the VAF is defined as follows:

$$\text{VAF} = \left[1 - \frac{\text{var}\left(CoSGPoC_i - CoS\hat{G}PoC_i\right)}{\text{var}(CoSGPoC_i)}\right] \times 100 \tag{22}$$

The coefficient of determination, which is also often referred to as R^2, is a statistical indicator that is used for the aim of assessing the degree of linear relationship that exists between dataset parameters. The value of this coefficient is somewhere between one and zero.

$$R^2 = 1 - \frac{\sum_{i=1}^{n}\left(CoSGPoC_i - CoS\hat{G}PoC_i\right)^2}{\sum_{i=1}^{n}\left(CoSGPoC_i - CoS\hat{G}PoC_i\right)} \tag{23}$$

Here, n is the sample size and CoSGePC, CoSĜePC, and $\overline{\text{CoSGePC}}$ stand for the real CoSGePC, the expected CoSGePC, and the mean CoSGePC, respectively. The variable n represents the sample size while the variables and CoSGePC represent the actual CoSGePC, the predicted CoSGePC, and the mean CoSGePC, respectively.

Hybrid RF Model and Background

We present the process of constructing and estimating the suggested hybrid RF CoS-GePC prediction model, which can be broken down into four steps:

1.   In line with the Pareto principle, the database was first randomly split into two sets: the training set consisted of eighty percent of the total and the testing set consisted of twenty percent of the total. This division procedure was conducted based on the literature suggestions [130]. In order to construct the prediction models and assess the efficacy of the models that were already in place, it was required to follow these stages. The training-set-to-testing-set ratio is 4:1, and it is often used because it has a high degree of prediction efficiency [131,132]. In the phases that follow, which are discussed in more depth, this ratio is described.

2.   In order to reduce the effect of input variables having varying scales in the database and to save unnecessary computation costs, all datasets were normalized within the range of 0 and 1 [133].

3.   Both the total number of trees (n_{tree}) and the number of features used to construct each tree (m_{tree}) are ideal hyperparameters in the RF algorithm. The best RF models were found after searching for them using HHO and SCA.

4.   The next stage was to assess the accuracy of the predictions made by the RF models that had been constructed by comparing them to both the training set and the testing set. This was achieved with the use of a Taylor graph and four evaluation metrics, which were as follows: the mean absolute error (MAE), root mean square error (RMSE), variance adjusted for (VAF), and R^2.

5. Results and Discussions

5.1. Developed RF Model

The RF models' hyperparameters, m_{tree} and n_{tree}, were fine-tuned with the use of the HHO approach. The fitness function was determined by the RMSE of the prediction being made at different points in time, the population number of Harris hawks was modified

from 10 to 100 as shown in Table 4, and ten HHO-RF models were built with a maximum iteration of 1000. The best cost values for the ten best HHO-RF models varied from 0.174 to 0.847, as shown in Figure 8. The RF model with a population of 70 had the best cost of 0.174, suggesting that it was the most successful model in the validation sets. The population size of 200 had the greatest best cost, which gave the impression that the RF model did quite poorly in the validation sets in comparison to the other models.

Table 4. Performance of HHO algorithm with various population sizes.

Swarm Size	Training Phase				Testing Phase			
	R^2	RMSE	VAF	MAE	R^2	RMSE	VAF	MAE
10	0.9538	6.4831	92.91981	5.0884	0.9370	8.0403	92.1255	5.9976
20	0.9562	6.4819	93.2536	5.0874	0.9381	8.0177	92.1354	5.9882
30	0.9568	6.4810	93.3892	5.0873	0.9385	8.0120	92.1376	5.9856
40	0.9575	6.4745	93.6056	5.0863	0.9399	7.9476	92.1477	5.9768
50	0.9575	6.4742	93.8128	5.0860	0.9400	7.9439	92.1452	5.9767
60	0.9545	6.4823	93.1716	5.0880	0.9373	8.0249	92.1322	5.9900
70	0.9576	6.4738	93.8773	5.0854	0.9400	7.9145	92.1498	5.9655
80	0.9569	6.4796	93.5313	5.0871	0.9388	7.9491	92.1449	5.9842
90	0.9552	6.4822	93.2250	5.0874	0.9376	8.0178	92.1364	5.9891
100	0.9542	6.4829	93.0451	5.0882	0.9371	8.0295	92.1264	5.9962
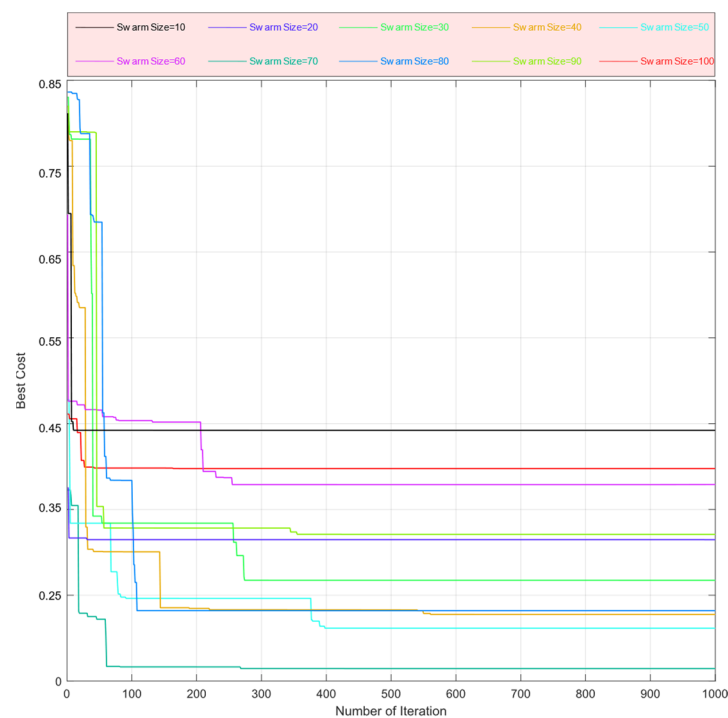
Figure 8. Convergence plot of HHO-RF model.

The optimal population size should not be determined just by examining fitness curves. Table 5 shows our comprehensive rating of the test and training sets' index values, which we used to choose the best of ten HHO-RF models. The optimal population values for the HHO-RF model were as shown in Table 5. In the training set, the R^2 was 0.9576, RMSE was 6.4738, VAF was 93.8773, and MAE was 5.0854. In the testing set, the R^2 was 0.94, RMSE was 7.9145, VAF was 92.1498, and MAE was 5.9655.

Table 5. Rating ten HHO-RF models to find the best one.

Swarm Size	Training Phase				Testing Phase				Total Rate	Rank
	R^2	RMSE	VAF	MAE	R^2	RMSE	VAF	MAE		
10	1	1	1	1	1	1	1	1	8	10
20	5	5	5	5	5	5	4	5	39	6
30	6	6	6	6	6	6	6	6	48	5
40	8	8	8	8	8	8	9	8	65	3
50	9	9	9	9	9	9	8	9	71	2
60	3	3	3	3	3	3	3	3	24	8
70	10	10	10	10	10	10	10	10	80	1
80	7	7	7	7	7	7	7	7	56	4
90	4	4	4	4	4	4	5	4	33	7
100	2	2	2	2	2	2	2	2	16	9

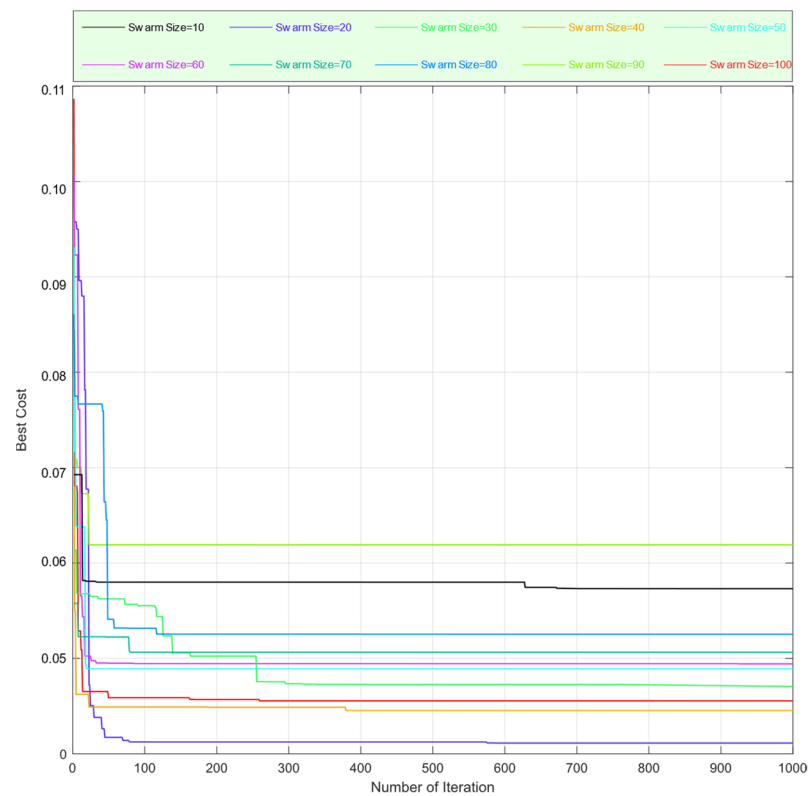For the aim of SCA-RF modeling, ten models were constructed with a maximum iteration of 1000. There were 10, 20, 30, 40, 50, 60, 70, 80, 90, and 100 individuals in the populations as shown in Table 6. The training and testing data for these models were identical to those used for the HHO-RF model used. The iterative procedure of the top 10 HHO-RF models is shown in Figure 9. The fitness values fell between 0.018 and 0.108, and the 20-and 40-population SCA-RF model outperformed the others in the validation suite. Lastly, according to the detailed rankings in Table 7, the best number of search agents for the SCA-RF model was 20. On the training set, this yielded the following values: $R^2 = 0.9849$, RMSE = 4.3511, VAF = 96.8187, and MAE = 2.762. On the testing set, the values were thus: $R^2 = 0.9646$, RMSE = 5.6707, VAF = 95.0266, and MAE = 2.761. When compared to population numbers in other contexts, this one was better. Consequently, the SCA-RF model with 20 search agents and the HHO-RF model with 70 populations were the most successful models for CoSGePC forecasting. Both of these models were given a green light.

Table 6. Performance of SCA algorithm with various population sizes.

Swarm Size	Training Phase				Testing Phase			
	R^2	RMSE	VAF	MAE	R^2	RMSE	VAF	MAE
10	0.9811	4.3900	96.7931	2.7650	0.9615	5.7078	95.0023	2.7649
20	0.9849	4.3511	96.8187	2.7620	0.9646	5.6707	95.0266	2.7610
30	0.9842	4.3606	96.8128	2.7637	0.9634	5.6765	95.0216	2.7619
40	0.9848	4.3591	96.8158	2.7626	0.9645	5.6733	95.0220	2.7613
50	0.9841	4.3614	96.7981	2.7639	0.9631	5.6836	95.0144	2.7625
60	0.9835	4.3678	96.8123	2.7640	0.9627	5.6883	95.0122	2.7626
70	0.9825	4.3764	96.7978	2.7640	0.9622	5.6991	95.0132	2.7634
80	0.9818	4.3798	96.7972	2.7645	0.9618	5.7027	95.0090	2.7637
90	0.9815	4.3888	96.7958	2.7648	0.9617	5.7063	95.0032	2.7640
100	0.9848	4.3591	96.8156	2.7629	0.9645	5.6765	95.0245	2.7614

Table 7. Rating ten SCA-RF models to find the best one.

Swarm Size	Training Phase				Testing Phase				Total Rate	Rank
	R^2	RMSE	VAF	MAE	R^2	RMSE	VAF	MAE		
10	1	1	1	1	1	1	1	1	8	10
20	10	10	10	10	10	10	10	10	80	1
30	7	7	7	7	7	7	7	7	56	4
40	9	9	9	9	9	9	8	9	71	2
50	6	6	5	6	6	6	6	6	47	5
60	5	5	6	5	5	5	4	5	40	6
70	4	4	4	4	4	4	5	4	33	7
80	3	3	3	3	3	3	3	3	24	8
90	2	2	2	2	2	2	2	2	16	9

Figure 9. Convergence plot of SCA-RF model.

5.2. Comparison with Other AI Techniques

To compare our models, we utilized various other models including the Multilayer Perceptron (MLP), Classification and Regression Tree (CART), Least Squares Support Vector Machine (LSSVM), Multivariate Adaptive Regression Splines (MARS), and Extreme Learning Machine (ELM). There are noticeable variations in performance across a number of statistical measures when comparing different AI methods for predicting concrete qualities such as the R^2, RMSE, VAF, and MAE. Among the models evaluated, the RF-SCA model exhibited the highest performance during both training and testing phases as shown in Tables 8 and 9, achieving R^2 values of 0.9825 and 0.9622, respectively. It also demonstrated the lowest RMSE (4.3764 in training and 5.6991 in testing) and MAE (2.7640 in training and 3.7634 in testing), indicating its robustness and accuracy. Following closely, the Random Forest with Harris Hawks Optimization (RF-HHO) model was the second-best model, with R^2 values of 0.9576 in training and 0.9400 in testing, though it had slightly higher RMSE and MAE values compared to RF-SCA.

Table 8. Statistical indices for developed AI models in predicting CoSGePC.

Model	Training				Testing			
	R^2	RMSE	VAF	MAE	R^2	RMSE	VAF	MAE
RF-SCA	0.9825	4.3764	96.7978	2.7640	0.9622	5.6991	95.0132	3.7634
RF-HHO	0.9576	6.4738	93.8773	5.0854	0.9400	7.9145	92.1498	5.9655
MLP	0.9499	7.6078	92.8789	6.8854	0.9385	8.2455	91.1510	7.0455
CART	0.9289	9.9218	90.8784	7.8654	0.9117	11.0925	87.1514	9.6755
LSSVM	0.9519	6.9218	93.8790	5.6154	0.9314	9.0205	91.0509	8.2355
MARS	0.9091	10.6518	87.8784	8.9254	0.8812	11.1365	86.1514	11.5055
ELM	0.9228	9.9318	89.8785	8.4754	0.9115	12.0585	85.1509	12.2155

Table 9. Rating of developed AI models to find the best one.

Model	Training				Testing				Total Rate	Rank
	R^2	RMSE	VAF	MAE	R^2	RMSE	VAF	MAE		
RF-SCA	7	7	7	7	7	7	7	7	56	1
RF-HHO	6	6	5	6	6	6	6	6	47	2
MLP	4	4	4	4	5	5	5	5	36	4
CART	3	3	3	3	3	3	3	3	24	5
LSSVM	5	5	6	5	4	4	4	4	37	3
MARS	1	1	1	1	1	2	2	2	11	7
ELM	2	2	2	2	2	1	1	1	13	6

The Multilayer Perceptron (MLP) model, while less accurate than the random forest models, performed reasonably well with R^2 values of 0.9499 (training) and 0.9385 (testing). However, it exhibited higher RMSE and MAE values, indicating reduced precision. Other models, including the Classification and Regression Tree (CART), Least Squares Support Vector Machine (LSSVM), Multivariate Adaptive Regression Splines (MARS), and Extreme Learning Machine (ELM), showed lower performance. Specifically, CART and MARS had the lowest R^2 values and the highest RMSE and MAE during both training and testing phases, suggesting they were the least effective models for this task. Hence, these results underscore the effectiveness of ensemble methods, particularly RF-SCA and RF-HHO, in accurately predicting the properties of concrete. The variation in performance across different AI techniques highlights the superiority of ensemble models over single models in this context.

Figure 10 illustrates the outcomes of the predictions made by the models that were implemented. Due to the same scale being used by all the models, the area of each bubble is directly proportional to the absolute error (AE), which was calculated using the following formula:

$$AE = \left| CoSGePC - Co\hat{S}GePC \right| \tag{24}$$

The above depicts the actual CoSGePC and predicted CoSGePC, where AE stands for the absolute error. Compared to the three traditional models, the two hybrid RF models performed far better. To provide a more accurate assessment of their prediction skills, Figure 11 gives a comprehensive rating of all the models that are being compared. When comparing performance across training and testing datasets, the SCA-RF model was clearly superior. On the former, it achieved an R^2 of 0.9849, RMSE of 4.3511, VAF of 96.8187, and MAE of 2.762 for the training set and an R^2 of 0.9646, RMSE of 5.6707, VAF of 95.0266, and MAE of 2.761 for the testing set. On the latter, the results were even more impressive.

Using a two-dimensional plane, Taylor [134] created a graph that accurately and intuitively displays prediction performance. The graph reflects three-dimensional data. In order to compare the prediction performance of different models and to confirm that hybrid RF models are better, the Taylor graph (Figure 12) is used as an assessment indication. The models used for this purpose are the standard deviation, the root mean squared deviation, and the correlation coefficient. The most accurate model in terms of prediction is the one that is closest to the purple point in Figure 12. Figure 12 shows that all of the models save the hybrid RF ones performed poorly. This was particularly true of the SCA-RF model. In conclusion, between training and testing, the SCA-RF model performed the best in predicting CoSGePC, and it is, therefore, the model that is suggested.
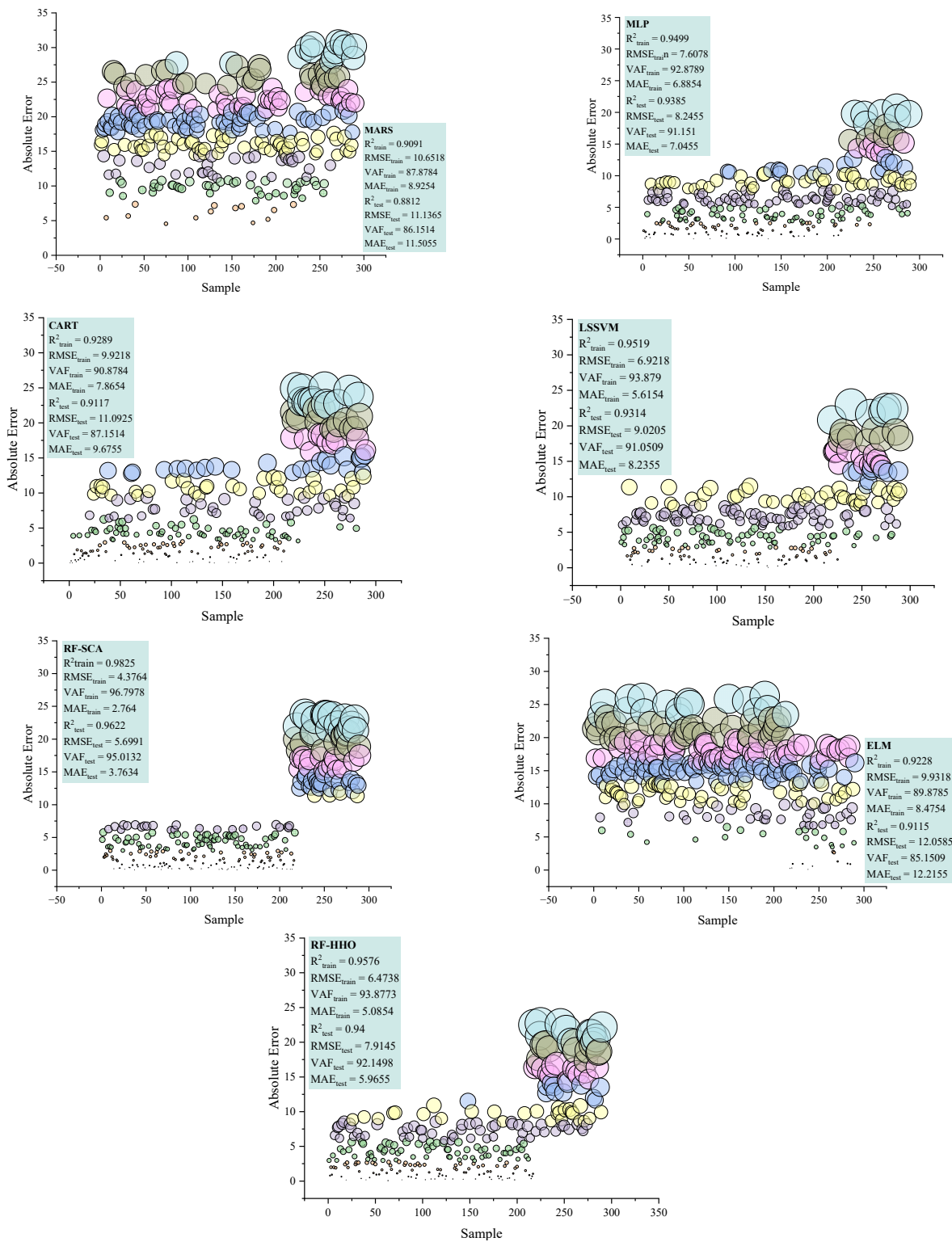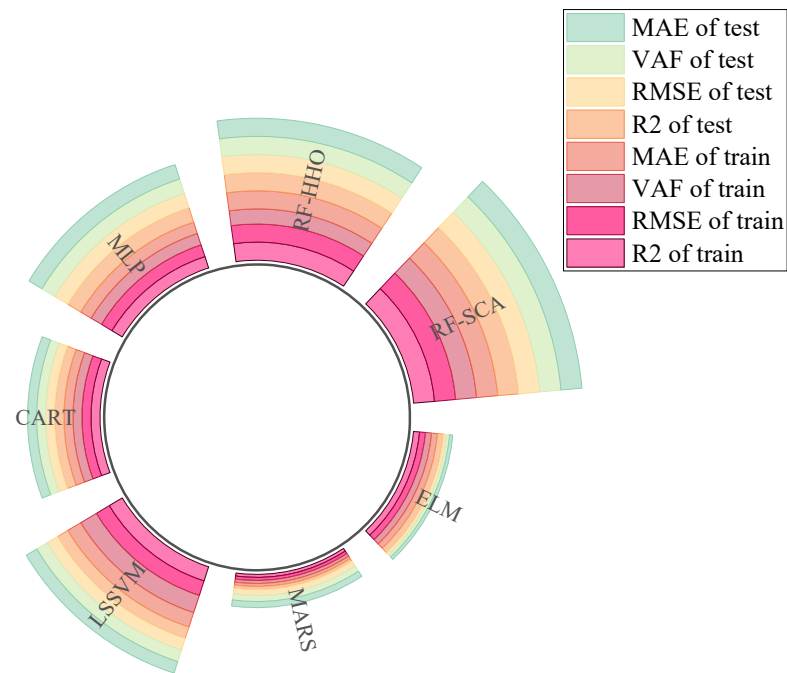
Figure 10. Prediction error analysis of the models.

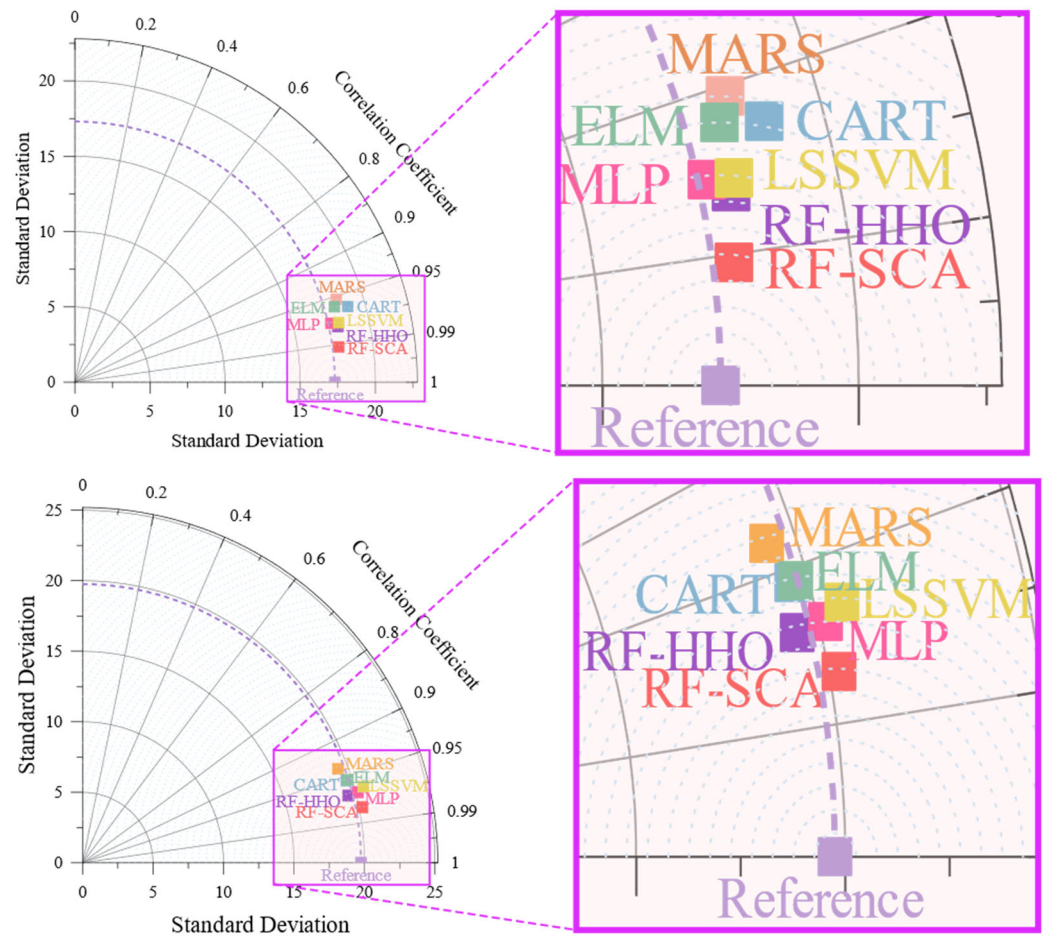**Figure 11.** Comprehensive rankings of CoSGePC estimation techniques.

Figure 12. Taylor diagram to show performance of developed models in training (**above**) and testing (**below**) phases.

5.3. Comparison with Literature Models

The paper's findings are contrasted with previous reports to assess different model performances. Table 10 summarizes the methods, data point counts, and R^2 values across various studies. The evaluation demonstrates the efficiency of the models employed in this research. The analysis reveals that the models utilized in this research are extremely efficient. In our research, the HHO-RF model obtained an R^2 value of 0.9576, which was similar to the top R^2 values mentioned in prior studies, like the 0.9909 and 0.99 by Azimi-Pour et al. [69] and Farooq et al. [73], respectively. Furthermore, our HHO-RF model outperformed numerous models in the literature by achieving the highest R^2 value of 0.9825. More advanced hybrid methods such as HHO-RF and SCA-RF demonstrated better results in comparison to individual techniques like SVM and GEP that had been utilized in prior research. This indicates that metaheuristic optimization algorithms can effectively fine-tune the hyperparameters of models. In our research, the LSSVM and MLP models showed strong performance, achieving R^2 values of 0.9519 and 0.9499, respectively. These values were on par with those of other methods in the research, like the R^2 of 0.966 achieved by Emad et al. [90] in an ANN model. Therefore, the models created in this research, specifically the HHO-RF and SCA-RF models, show a high level of predictive accuracy with R^2 values that are on par with or better than those found in existing studies. This shows the possibility of boosting model performance by incorporating metaheuristic optimization algorithms, even with limited data.

Table 10. Comparison of our proposed model with literature models for estimating CoSGePC.

Author	Year	Technique	Number of Data	R^2
Huang et al. [54]	2021	SVM	114	0.947
Sarir et al. [55]	2019	GEP	303	0.939
Ahmad et al. [57]	2021	GEP, ANN, DT	642	0.88
Azimi-Pour et al. [58]	2020	SVM	-	0.9909
Saha et al. [59]	2020	SVM	115	0.955
Hahmansouri et al. [60]	2019	GEP	54	0.9071
Aslam et al. [61]	2020	GEP	357	0.957
Farooq et al. [62]	2020	RF and GEP	357	0.99
Belalia Douma et al. [69]	2017	ANN	114	0.95
Javad et al. [74]	2020	GEP	277	0.99
Güçlüer et al. [76]	2021	ANN, SVM, DT	100	0.86
Emad et al. [79]	2022	ANN, M5P,	306	0.966
Kuma et al. [81]	2022	GPR, SVMR	194	0.9803
Jaf et al. [82]	2023	NLR, MLR, ANN	236	0.987
Ali et al. [84]	2023	LR, MLR, NLR, PQ, IA, FQ	420	0.96
Our Model	2024	RF-SCA, RF-HHO, MLP, CART, LSSVM, MARS, and ELM	290	0.9825, 0.9576, 0.9499, 0.9289, 0.9519, 0.9091, and 0.9228

5.4. Sensitivity Analysis

Due to its lower carbon emissions and increased durability, GePC has become a widely recognized sustainable substitute for conventional concrete. This highlights the critical need of investigating the interrelationships between input and output attributes in detail. Zhang et al. (2020a) [135] said that the sensitivity analysis for the RF approach was conducted using an internal computation of the Gini index. A higher Gini index indicates that the CoSGePC is more sensitive to the value of an input parameter [86]. There has to be some thought given to this. Therefore, during the last phase of this research, the parameters that had the most and least influence on determining CoSGePC were pinpointed. In order to achieve this, the researchers utilized a sensitivity analysis technique. This approach evaluates how strong the connection is between every set of influential factors on CoSGePC. The below equation is used for this purpose [136]:

$$r(I, u) = \frac{\sum\limits_{i=1}^{n} (I_{k,i} - \overline{I}_k) \cdot (u_i - \overline{u})}{\sqrt{\sum\limits_{i=1}^{n} (I_{k,i} - \overline{I}_k)^2 \cdot \sum\limits_{i=1}^{n} (u_i - \overline{u})^2}} \tag{25}$$

A larger r value signifies that the inputs have a stronger impact on the target parameter. Figure 13 suggests that the FA, NaOH molarity, and Gravel 4/10 mm have a negative impact on the severity of CoGePC while the other input parameters have a positive impact on CoGePC outcomes. The impact of the WS ratio is smaller compared to those of all parameters (r = 0.125), with GGBS (r = 0.456) being the most significant factor affecting the CoGePC. Furthermore, the smallest-to-largest ranking of parameters based on the r values is as follows: WS < Na_2SiO_3 < NaOH molarity < FAg < Gravel 4/10 < Gravel 10/20 < FA < GGBS with corresponding impacts of −0.421, −0.264, −0.215, 0.125, 0.176, 0.237, 0.336, and 0.456.
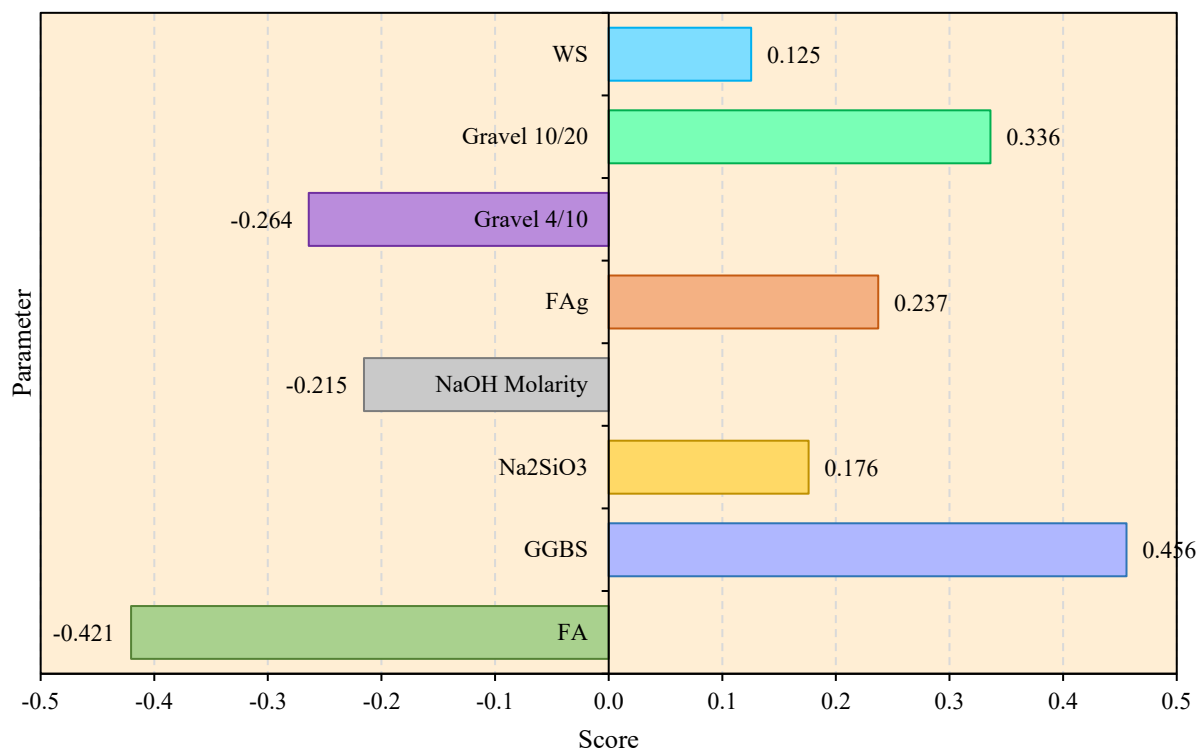
Figure 13. The effective parameters and their importance.

5.5. Limitations

In our research, we utilized different soft computing methods such as the MLP, CART, LSSVM, MARS, and ELM and their combinations (SCA-RF and HHO-RF) to anticipate the CoSGePC. Although these methods showed impressive results in forecasting the CoS-GePC, it is important to acknowledge their inherent restrictions. The intricate optimization processes and numerous parameters are key aspects of the hybrid models, especially of SCA-RF and HHO-RF. The complexity of these models can reduce their interpretability compared to simpler methods, potentially restricting their practical use and comprehension. Moreover, dataset quality and quantity play a crucial role in determining the accuracy and effectiveness of the soft computing models. Our research used a modest dataset of 290 samples, potentially impacting the results' generalizability. The benefits of employing these models include their ability to capture complex relationships in the data and provide high predictive accuracy under optimal conditions. However, their limitations also encompass the risk of overfitting and sensitivity to the chosen hyperparameters. Bigger and more varied datasets may offer a more thorough assessment of the models' effectiveness. The effectiveness of these models greatly depends on the selected hyperparameters and optimization algorithms. Differences in the number of swarms and other factors can greatly

affect the outcomes, as shown by the varying R^2 values in various models and swarm sizes. Moreover, the models were finely adjusted to forecast the CoSGePC using specific input parameters. Additionally, while the models were finely adjusted to forecast the CoSGePC using specific input parameters, the lack of extensive validation across different datasets may have hindered their robustness. Even though the outcomes look positive, additional validation and adjustments might be needed to apply these models to various concrete types or construction materials. In order to provide a comprehensive overview of the strengths and weaknesses of the soft computing methods employed in our research, we present a summary in Table 11. This table outlines the key benefits and limitations associated with these methods, highlighting their predictive accuracy and flexibility and the impact of dataset quality on their performance.

Table 11. Benefits and limitations of soft computing methods for forecasting CoSGePC.

Aspect	Benefits	Limitations
Predictive accuracy	High predictive accuracy under optimal conditions.	Risk of overfitting if models are not properly validated.
Complex relationships	Ability to capture complex relationships in data.	Complexity can reduce interpretability compared to simpler methods.
Flexibility	Adaptable to various types of data and can be tailored for specific applications.	Performance highly dependent on the choice of hyperparameters and optimization algorithms.
Model combinations	Hybrid models (SCA-RF and HHO-RF) can enhance prediction performance by combining strengths of multiple algorithms.	Increased complexity can hinder practical use and comprehension.
Data utilization	Can handle nonlinear relationships effectively.	Limited by dataset quality and size; a modest dataset of 290 samples may impact generalizability.
Robustness	Potential for robustness if adequately trained on diverse datasets.	Lack of extensive validation across different datasets may hinder robustness for varied applications.

6. Conclusions and Future Works

This paper highlights the effectiveness of advanced machine learning techniques, particularly hybrid models, in forecasting geopolymer composite compressive strength. The integration of Harris Hawks Optimization (HHO) and the Sine Cosine Algorithm (SCA) with Random Forest (RF) models has demonstrated significant improvements in predictive accuracy compared to traditional methods and classical models. The SCA-RF model, with an RMSE of 1.562 and an R^2 of 0.987, emerged as the most accurate model, indicating its robustness in capturing the complex relationships between input variables and the geopolymer composites' compressive strength. The HHO-RF model also showed strong performance, with an RMSE of 1.742 and an R^2 of 0.982, further validating the efficacy of hybrid approaches. In comparison, traditional machine learning models effectiveness such as the ELM, GRNN, and RBF were not reliable, with higher RMSE values and lower R^2 scores. Specifically, the ELM model had an RMSE of 3.812 and an R^2 of 0.921, the GRNN model had an RMSE of 4.130 and an R^2 of 0.907, and the RBF model had an RMSE of 3.964 and an R^2 of 0.915. These findings underscore the promising future of using hybrid ML models to improve prediction model accuracy in the field of sustainable construction materials. By enabling precise predictions of compressive strength, these models can facilitate the optimization of mix designs, reduce experimental efforts, and promote the adoption of environmentally friendly construction practices. This research contributes to the ongoing efforts to develop sustainable and efficient construction materials, aligning with global initiatives to reduce the environmental impact of the construction industry.

References

1. Chen, Y.; Liu, P.; Sha, F.; Yu, Z.; He, S.; Xu, W.; Lv, M. Effects of Type and Content of Fibers, Water-to-Cement Ratio, and Cementitious Materials on the Shrinkage and Creep of Ultra-High Performance Concrete. *Polymers* **2022**, *14*, 1956. [CrossRef] [PubMed]
2. Khan, M.; Cao, M.; Hussain, A.; Chu, S.H. Effect of Silica-Fume Content on Performance of CaCO3 Whisker and Basalt Fiber at Matrix Interface in Cement-Based Composites. *Constr. Build. Mater.* **2021**, *300*, 124046. [CrossRef]
3. Khan, M.; Cao, M.; Chaopeng, X.; Ali, M. Experimental and Analytical Study of Hybrid Fiber Reinforced Concrete Prepared with Basalt Fiber under High Temperature. *Fire Mater.* **2022**, *46*, 205–226. [CrossRef]
4. Biricik, H.; Kırgız, M.S.; Galdino, A.G.d.S.; Kenai, S.; Mirza, J.; Kinuthia, J.; Ashteyat, A.; Khitab, A.; Khatib, J. Activation of Slag through a Combination of NaOH/NaS Alkali for Transforming It into Geopolymer Slag Binder Mortar—Assessment the Effects of Two Different Blaine Fines and Three Different Curing Conditions. *J. Mater. Res. Technol.* **2021**, *14*, 1569–1584. [CrossRef]
5. Mahmood, A.; Noman, M.T.; Pechočiaková, M.; Amor, N.; Petrů, M.; Abdelkader, M.; Militký, J.; Sozcu, S.; Ul Hassan, S.Z. Geopolymers and Fiber-reinforced Concrete Composites in Civil Engineering. *Polymers* **2021**, *13*, 2099. [CrossRef]
6. Farooq, F.; Jin, X.; Javed, M.F.; Akbar, A.; Shah, M.I.; Aslam, F.; Alyousef, R. Geopolymer Concrete as Sustainable Material: A State of the Art Review. *Constr. Build. Mater.* **2021**, *306*, 124762. [CrossRef]
7. Ahmed, M.; Bashar, I.; Alam, S.T.; Wasi, A.I.; Jerin, I.; Khatun, S.; Rahman, M. An Overview of Asian Cement Industry: Environmental Impacts, Research Methodologies and Mitigation Measures. *Sustain. Prod. Consum.* **2021**, *28*, 1018–1039. [CrossRef]
8. Tariq, H.; Siddique, R.M.A.; Shah, S.A.R.; Azab, M.; Attiq-Ur-rehman; Qadeer, R.; Ullah, M.K.; Iqbal, F. Mechanical Performance of Polymeric ARGF-Based Fly Ash-Concrete Composites: A Study for Eco-Friendly Circular Economy Application. *Polymers* **2022**, *14*, 1774. [CrossRef]
9. Alhazmi, H.; Shah, S.A.R.; Anwar, M.K.; Raza, A.; Ullah, M.K.; Iqbal, F. Utilization of Polymer Concrete Composites for a Circular Economy: A Comparative Review for Assessment of Recycling and Waste Utilization. *Polymers* **2021**, *13*, 2135. [CrossRef]
10. Khan, M.; Rehman, A.; Ali, M. Efficiency of Silica-Fume Content in Plain and Natural Fiber Reinforced Concrete for Concrete Road. *Constr. Build. Mater.* **2020**, *244*, 118382. [CrossRef]
11. Ahmad, W.; Ahmad, A.; Ostrowski, K.A.; Aslam, F.; Joyklad, P.; Zajdel, P. Sustainable Approach of Using Sugarcane Bagasse Ash in Cement-Based Composites: A Systematic Review. *Case Stud. Constr. Mater.* **2021**, *15*, e00698. [CrossRef]
12. Snoeck, D.; Jensen, O.M.; De Belie, N. The Influence of Superabsorbent Polymers on the Autogenous Shrinkage Properties of Cement Pastes with Supplementary Cementitious Materials. *Cem. Concr. Res.* **2015**, *74*, 59–67. [CrossRef]
13. Thomas, B.S.; Yang, J.; Bahurudeen, A.; Abdalla, J.A.; Hawileh, R.A.; Hamada, H.M.; Nazar, S.; Jittin, V.; Ashish, D.K. Sugarcane Bagasse Ash as Supplementary Cementitious Material in Concrete—A Review. *Mater. Today Sustain.* **2021**, *15*, 100086. [CrossRef]
14. Hefni, Y.; Zaher, Y.A.E.; Wahab, M.A. Influence of Activation of Fly Ash on the Mechanical Properties of Concrete. *Constr. Build. Mater.* **2018**, *172*, 728–734. [CrossRef]
15. Zaghloul, M.M.Y.; Mohamed, Y.S.; El-Gamal, H. Fatigue and Tensile Behaviors of Fiber-Reinforced Thermosetting Composites Embedded with Nanoparticles. *J. Compos. Mater.* **2019**, *53*, 709–718. [CrossRef]
16. Mahmoud Zaghloul, M.Y.; Yousry Zaghloul, M.M.; Yousry Zaghloul, M.M. Developments in Polyester Composite Materials—An in-Depth Review on Natural Fibres and Nano Fillers. *Compos. Struct.* **2021**, *278*, 114698. [CrossRef]
17. Han, X.; Yang, J.; Feng, J.; Zhou, C.; Wang, X. Research on Hydration Mechanism of Ultrafine Fly Ash and Cement Composite. *Constr. Build. Mater.* **2019**, *227*, 116697. [CrossRef]
18. Zhou, Z.; Sofi, M.; Liu, J.; Li, S.; Zhong, A.; Mendis, P. Nano-CSH Modified High Volume Fly Ash Concrete: Early-Age Properties and Environmental Impact Analysis. *J. Clean. Prod.* **2021**, *286*, 124924. [CrossRef]
19. Pacheco-Torgal, F.; Castro-Gomes, J.; Jalali, S. Alkali-Activated Binders: A Review. Part 1. Historical Background, Terminology, Reaction Mechanisms and Hydration Products. *Constr. Build. Mater.* **2008**, *22*, 1305–1314. [CrossRef]
20. Mohamed, O.A. A Review of Durability and Strength Characteristics of Alkali-Activated Slag Concrete. *Materials* **2019**, *12*, 1198. [CrossRef]

21. Peng, Y.; Unluer, C. Analyzing the Mechanical Performance of Fly Ash-Based Geopolymer Concrete with Different Machine Learning Techniques. *Constr. Build. Mater.* **2022**, *316*, 125785. [CrossRef]

22. Algaifi, H.A.; Mohamed, A.M.; Alsuhaibani, E.; Shahidan, S.; Alrshoudi, F.; Huseien, G.F.; Bakar, S.A. Optimisation of Gbfs, Fly Ash, and Nano-Silica Contents in Alkali-Activated Mortars. *Polymers* **2021**, *13*, 2750. [CrossRef] [PubMed]

23. Ahmad, A.; Ahmad, W.; Aslam, F.; Joyklad, P. Compressive Strength Prediction of Fly Ash-Based Geopolymer Concrete via Advanced Machine Learning Techniques. *Case Stud. Constr. Mater.* **2022**, *16*, e00840. [CrossRef]

24. Wong, L.S. Durability Performance of Geopolymer Concrete: A Review. *Polymers* **2022**, *14*, 868. [CrossRef] [PubMed]

25. Okoye, F.N. Geopolymer Binder: A Veritable Alternative to Portland Cement. *Mater. Today Proc.* **2017**, *4*, 5599–5604. [CrossRef]

26. Komnitsas, K.; Zaharaki, D. Geopolymerisation: A Review and Prospects for the Minerals Industry. *Miner. Eng.* **2007**, *20*, 1261–1277. [CrossRef]

27. Cao, M.; Mao, Y.; Khan, M.; Si, W.; Shen, S. Different Testing Methods for Assessing the Synthetic Fiber Distribution in Cement-Based Composites. *Constr. Build. Mater.* **2018**, *184*, 128–142. [CrossRef]

28. Sadrmomtazi, A.; Sobhani, J.; Mirgozar, M.A. Modeling Compressive Strength of EPS Lightweight Concrete Using Regression, Neural Network and ANFIS. *Constr. Build. Mater.* **2013**, *42*, 205–216. [CrossRef]

29. Nafees, A.; Amin, M.N.; Khan, K.; Nazir, K.; Ali, M.; Javed, M.F.; Aslam, F.; Musarat, M.A.; Vatin, N.I. Modeling of Mechanical Properties of Silica Fume-Based Green Concrete Using Machine Learning Techniques. *Polymers* **2022**, *14*, 30. [CrossRef]

30. Nafees, A.; Khan, S.; Javed, M.F.; Alrowais, R.; Mohamed, A.M.; Mohamed, A.; Vatin, N.I. Forecasting the Mechanical Properties of Plastic Concrete Employing Experimental Data Using Machine Learning Algorithms: DT, MLPNN, SVM, and RF. *Polymers* **2022**, *14*, 1583. [CrossRef]

31. Ilyas, I.; Zafar, A.; Afzal, M.T.; Javed, M.F.; Alrowais, R.; Althoey, F.; Mohamed, A.M.; Mohamed, A.; Vatin, N.I. Advanced Machine Learning Modeling Approach for Prediction of Compressive Strength of FRP Confined Concrete Using Multiphysics Genetic Expression Programming. *Polymers* **2022**, *14*, 1789. [CrossRef] [PubMed]

32. Wu, M.; Qi, C.; Derrible, S.; Choi, Y.; Fourie, A.; Ok, Y.S. Regional and Global Hotspots of Arsenic Contamination of Topsoil Identified by Deep Learning. *Commun. Earth Environ.* **2024**, *5*, 10. [CrossRef]

33. Qi, C.; Wu, M.; Liu, H.; Liang, Y.; Liu, X.; Lin, Z. Machine Learning Exploration of the Mobility and Environmental Assessment of Toxic Elements in Mining-Associated Solid Wastes. *J. Clean. Prod.* **2023**, *401*, 136771. [CrossRef]

34. Zhou, M.; Hu, T.; Wu, M.; Ma, C.; Qi, C. Rapid Estimation of Soil Mn Content by Machine Learning and Soil Spectra in Large-Scale. *Ecol. Inform.* **2024**, *81*, 102615. [CrossRef]

35. Xu, X.; Qi, C.; Aretxabaleta, X.M.; Ma, C.; Spagnoli, D.; Manzano, H. The Initial Stages of Cement Hydration at the Molecular Level. *Nat. Commun.* **2024**, *15*, 2731. [CrossRef]

36. Jiskani, I.M.; Yasli, F.; Hosseini, S.; Rehman, A.U.; Uddin, S. Improved Z-Number Based Fuzzy Fault Tree Approach to Analyze Health and Safety Risks in Surface Mines. *Resour. Policy* **2022**, *76*, 102591. [CrossRef]

37. Jiskani, I.M.; Zhou, W.; Hosseini, S.; Wang, Z. Mining 4.0 and Climate Neutrality: A Unified and Reliable Decision System for Safe, Intelligent, and Green & Climate-Smart Mining. *J. Clean. Prod.* **2023**, *410*, 137313. [CrossRef]

38. Zhang, Z.; Hosseini, S.; Monjezi, M.; Yari, M. Extension of Reliability Information of Z-Numbers and Fuzzy Cognitive Map: Development of Causality-Weighted Rock Engineering System to Predict and Risk Assessment of Blast-Induced Rock Size Distribution. *Int. J. Rock Mech. Min. Sci.* **2024**, *178*, 105779. [CrossRef]

39. Öztaş, A.; Pala, M.; Özbay, E.; Kanca, E.; Çağlar, N.; Bhatti, M.A. Predicting the Compressive Strength and Slump of High Strength Concrete Using Neural Network. *Constr. Build. Mater.* **2006**, *20*, 769–775. [CrossRef]

40. Sobhani, J.; Najimi, M.; Pourkhorshidi, A.R.; Parhizkar, T. Prediction of the Compressive Strength of No-Slump Concrete: A Comparative Study of Regression, Neural Network and ANFIS Models. *Constr. Build. Mater.* **2010**, *24*, 709–718. [CrossRef]

41. Awoyera, P.O.; Kirgiz, M.S.; Viloria, A.; Ovallos-Gazabon, D. Estimating Strength Properties of Geopolymer Self-Compacting Concrete Using Machine Learning Techniques. *J. Mater. Res. Technol.* **2020**, *9*, 9016–9028. [CrossRef]

42. Hodhod, O.A.; Ahmed, H.I. Modeling the Corrosion Initiation Time of Slag Concrete Using the Artificial Neural Network. *HBRC J.* **2014**, *10*, 231–234. [CrossRef]

43. Chou, J.S.; Tsai, C.F.; Pham, A.D.; Lu, Y.H. Machine Learning in Concrete Strength Simulations: Multi-Nation Data Analytics. *Constr. Build. Mater.* **2014**, *73*, 771–780. [CrossRef]

44. Kabiru, O.A.; Owolabi, T.O.; Ssennoga, T.; Olatunji, S.O. Performance Comparison of SVM and ANN in Predicting Compressive Strength of Concrete. *IOSR J. Comput. Eng.* **2014**, *16*, 88–94.

45. Yeh, I.C.; Lien, L.C. Knowledge Discovery of Concrete Material Using Genetic Operation Trees. *Expert Syst. Appl.* **2009**, *36*, 5807–5812. [CrossRef]

46. Mustapha, I.B.; Abdulkareem, M.; Jassam, T.M.; AlAteah, A.H.; Al-Sodani, K.A.A.; Al-Tholaia, M.M.H.; Nabus, H.; Alih, S.C.; Abdulkareem, Z.; Ganiyu, A. Comparative Analysis of Gradient-Boosting Ensembles for Estimation of Compressive Strength of Quaternary Blend Concrete. *Int. J. Concr. Struct. Mater.* **2024**, *18*, 20. [CrossRef]

47. Alhakeem, Z.M.; Jebur, Y.M.; Henedy, S.N.; Imran, H.; Bernardo, L.F.A.; Hussein, H.M. Prediction of Ecofriendly Concrete Compressive Strength Using Gradient Boosting Regression Tree Combined with GridSearchCV Hyperparameter-Optimization Techniques. *Materials* **2022**, *15*, 7432. [CrossRef]

48. Faraz, M.I.; Arifeen, S.U.; Amin, M.N.; Nafees, A.; Althoey, F.; Niaz, A. A Comprehensive GEP and MEP Analysis of a Cement-Based Concrete Containing Metakaolin. *Structures* **2023**, *53*, 937–948. [CrossRef]

49. Shah, S.; Houda, M.; Khan, S.; Althoey, F.; Abuhussain, M.; Abuhussain, M.A.; Ali, M.; Alaskar, A.; Javed, M.F. Mechanical Behaviour of E-Waste Aggregate Concrete Using a Novel Machine Learning Algorithm: Multi Expression Programming (MEP). *J. Mater. Res. Technol.* **2023**, *25*, 5720–5740. [CrossRef]

50. Dey, A.; Rumman, R.; Wakjira, T.G.; Jindal, A.; Bediwy, A.G.; Islam, M.S.; Alam, M.S.; Al Martini, S.; Sabouni, R. Towards Net-Zero Emission: A Case Study Investigating Sustainability Potential of Geopolymer Concrete with Recycled Glass Powder and Gold Mine Tailings. *J. Build. Eng.* **2024**, *86*, 108683. [CrossRef]

51. Al Martini, S.; Sabouni, R.; Khartabil, A.; Wakjira, T.G.; Alam, M.S. Development and Strength Prediction of Sustainable Concrete Having Binary and Ternary Cementitious Blends and Incorporating Recycled Aggregates from Demolished UAE Buildings: Experimental and Machine Learning-Based Studies. *Constr. Build. Mater.* **2023**, *380*, 131278. [CrossRef]

52. Wakjira, T.G.; Kutty, A.A.; Alam, M.S. A Novel Framework for Developing Environmentally Sustainable and Cost-Effective Ultra-High-Performance Concrete (UHPC) Using Advanced Machine Learning and Multi-Objective Optimization Techniques. *Constr. Build. Mater.* **2024**, *416*, 135114. [CrossRef]

53. Wakjira, T.G.; Alam, M.S. Performance-Based Seismic Design of Ultra-High-Performance Concrete (UHPC) Bridge Columns with Design Example–Powered by Explainable Machine Learning Model. *Eng. Struct.* **2024**, *314*, 118346. [CrossRef]

54. Huang, J.; Sun, Y.; Zhang, J. Reduction of Computational Error by Optimizing SVR Kernel Coefficients to Simulate Concrete Compressive Strength through the Use of a Human Learning Optimization Algorithm. *Eng. Comput.* **2022**, *38*, 3151–3168. [CrossRef]

55. Sarir, P.; Chen, J.; Asteris, P.G.; Armaghani, D.J.; Tahir, M.M. Developing GEP Tree-Based, Neuro-Swarm, and Whale Optimization Models for Evaluation of Bearing Capacity of Concrete-Filled Steel Tube Columns. *Eng. Comput.* **2021**, *37*, 1–19. [CrossRef]

56. Balf, F.R.; Kordkheili, H.M.; Kordkheili, A.M. A New Method for Predicting the Ingredients of Self-Compacting Concrete (SCC) Including Fly Ash (FA) Using Data Envelopment Analysis (DEA). *Arab. J. Sci. Eng.* **2021**, *46*, 4439–4460. [CrossRef]

57. Ahmad, A.; Farooq, F.; Ostrowski, K.A.; Śliwa-Wieczorek, K.; Czarnecki, S. Application of Novel Machine Learning Techniques for Predicting the Surface Chloride Concentration in Concrete Containing Waste Material. *Materials* **2021**, *14*, 2297. [CrossRef]

58. Azimi-Pour, M.; Eskandari-Naddaf, H.; Pakzad, A. Linear and Non-Linear SVM Prediction for Fresh Properties and Compressive Strength of High Volume Fly Ash Self-Compacting Concrete. *Constr. Build. Mater.* **2020**, *230*, 117021. [CrossRef]

59. Saha, P.; Debnath, P.; Thomas, P. Prediction of Fresh and Hardened Properties of Self-Compacting Concrete Using Support Vector Regression Approach. *Neural Comput. Appl.* **2020**, *32*, 7995–8010. [CrossRef]

60. Shahmansouri, A.A.; Akbarzadeh Bengar, H.; Jahani, E. Predicting Compressive Strength and Electrical Resistivity of Eco-Friendly Concrete Containing Natural Zeolite via GEP Algorithm. *Constr. Build. Mater.* **2019**, *229*, 116883. [CrossRef]

61. Aslam, F.; Farooq, F.; Amin, M.N.; Khan, K.; Waheed, A.; Akbar, A.; Javed, M.F.; Alyousef, R.; Alabdulijabbar, H. Applications of Gene Expression Programming for Estimating Compressive Strength of High-Strength Concrete. *Adv. Civ. Eng.* **2020**, *2020*, 8850535. [CrossRef]

62. Farooq, F.; Amin, M.N.; Khan, K.; Sadiq, M.R.; Javed, M.F.; Aslam, F.; Alyousef, R. A Comparative Study of Random Forest and Genetic Engineering Programming for the Prediction of Compressive Strength of High Strength Concrete (HSC). *Appl. Sci.* **2020**, *10*, 7330. [CrossRef]

63. Asteris, P.G.; Kolovos, K.G. Self-Compacting Concrete Strength Prediction Using Surrogate Models. *Neural Comput. Appl.* **2019**, *31*, 409–424. [CrossRef]

64. Selvaraj, S.; Sivaraman, S. Prediction Model for Optimized Self-Compacting Concrete with Fly Ash Using Response Surface Method Based on Fuzzy Classification. *Neural Comput. Appl.* **2019**, *31*, 1365–1373. [CrossRef]

65. Zhang, J.; Ma, G.; Huang, Y.; sun, J.; Aslani, F.; Nener, B. Modelling Uniaxial Compressive Strength of Lightweight Self-Compacting Concrete Using Random Forest Regression. *Constr. Build. Mater.* **2019**, *210*, 713–719. [CrossRef]

66. Kaveh, A.; Bakhshpoori, T.; Hamze-Ziabari, S.M. M5' and Mars Based Prediction Models for Properties of Selfcompacting Concrete Containing Fly Ash. *Period. Polytech. Civ. Eng.* **2018**, *62*, 281–294. [CrossRef]

67. Sathyan, D.; Anand, K.B.; Prakash, A.J.; Premjith, B. Modeling the Fresh and Hardened Stage Properties of Self-Compacting Concrete Using Random Kitchen Sink Algorithm. *Int. J. Concr. Struct. Mater.* **2018**, *12*, 24. [CrossRef]

68. Vakhshouri, B.; Nejadi, S. Prediction of Compressive Strength of Self-Compacting Concrete by ANFIS Models. *Neurocomputing* **2018**, *280*, 13–22. [CrossRef]

69. Belalia Douma, O.; Boukhatem, B.; Ghrici, M.; Tagnit-Hamou, A. Prediction of Properties of Self-Compacting Concrete Containing Fly Ash Using Artificial Neural Network. *Neural Comput. Appl.* **2017**, *28*, 707–718. [CrossRef]

70. Abu Yaman, M.; Abd Elaty, M.; Taman, M. Predicting the Ingredients of Self Compacting Concrete Using Artificial Neural Network. *Alexandria Eng. J.* **2017**, *56*, 523–532. [CrossRef]

71. Ahmad, A.; Farooq, F.; Niewiadomski, P.; Ostrowski, K.; Akbar, A.; Aslam, F.; Alyousef, R. Prediction of Compressive Strength of Fly Ash Based Concrete Using Individual and Ensemble Algorithm. *Materials* **2021**, *14*, 794. [CrossRef] [PubMed]

72. Farooq, F.; Ahmed, W.; Akbar, A.; Aslam, F.; Alyousef, R. Predictive Modeling for Sustainable High-Performance Concrete from Industrial Wastes: A Comparison and Optimization of Models Using Ensemble Learners. *J. Clean. Prod.* **2021**, *292*, 126032. [CrossRef]

73. Bušić, R.; Benšić, M.; Miličević, I.; Strukar, K. Prediction Models for the Mechanical Properties of Self-Compacting Concrete with Recycled Rubber and Silica Fume. *Materials* **2020**, *13*, 1821. [CrossRef] [PubMed]

74. Javed, M.F.; Farooq, F.; Memon, S.A.; Akbar, A.; Khan, M.A.; Aslam, F.; Alyousef, R.; Alabduljabbar, H.; Rehman, S.K.U. New Prediction Model for the Ultimate Axial Capacity of Concrete-Filled Steel Tubes: An Evolutionary Approach. *Crystals* **2020**, *10*, 741. [CrossRef]

75. Nematzadeh, M.; Shahmansouri, A.A.; Fakoor, M. Post-Fire Compressive Strength of Recycled PET Aggregate Concrete Reinforced with Steel Fibers: Optimization and Prediction via RSM and GEP. *Constr. Build. Mater.* **2020**, *252*, 119057. [CrossRef]

76. Güçlüer, K.; Özbeyaz, A.; Göymen, S.; Günaydın, O. A Comparative Investigation Using Machine Learning Methods for Concrete Compressive Strength Estimation. *Mater. Today Commun.* **2021**, *27*, 102278. [CrossRef]

77. Ahmad, A.; Ostrowski, K.A.; Maślak, M.; Farooq, F.; Mehmood, I.; Nafees, A. Comparative Study of Supervised Machine Learning Algorithms for Predicting the Compressive Strength of Concrete at High Temperature. *Materials* **2021**, *14*, 4222. [CrossRef]

78. Asteris, P.G.; Skentou, A.D.; Bardhan, A.; Samui, P.; Pilakoutas, K. Predicting Concrete Compressive Strength Using Hybrid Ensembling of Surrogate Machine Learning Models. *Cem. Concr. Res.* **2021**, *145*, 106449. [CrossRef]

79. Emad, W.; Mohammed, A.S.; Kurda, R.; Ghafor, K.; Cavaleri, L.; Qaidi, S.M.A.; Hassan, A.M.T.; Asteris, P.G. Prediction of Concrete Materials Compressive Strength Using Surrogate Models. *Structures* **2022**, *46*, 1243–1267. [CrossRef]

80. Shen, Z.; Deifalla, A.F.; Kamiński, P.; Dyczko, A. Compressive Strength Evaluation of Ultra-High-Strength Concrete by Machine Learning. *Materials* **2022**, *15*, 3523. [CrossRef]

81. Kumar, A.; Arora, H.C.; Kapoor, N.R.; Mohammed, M.A.; Kumar, K.; Majumdar, A.; Thinnukool, O. Compressive Strength Prediction of Lightweight Concrete: Machine Learning Models. *Sustainability* **2022**, *14*, 2404. [CrossRef]

82. Jaf, D.K.I.; Abdulrahman, P.I.; Mohammed, A.S.; Kurda, R.; Qaidi, S.M.A.; Asteris, P.G. Machine Learning Techniques and Multi-Scale Models to Evaluate the Impact of Silicon Dioxide (SiO2) and Calcium Oxide (CaO) in Fly Ash on the Compressive Strength of Green Concrete. *Constr. Build. Mater.* **2023**, *400*, 132604.

83. Mahmood, W.; Mohammed, A.S.; Asteris, P.G.; Ahmed, H. Soft Computing Technics to Predict the Early-Age Compressive Strength of Flowable Ordinary Portland Cement. *Soft Comput.* **2023**, *27*, 3133–3150. [CrossRef]

84. Ali, R.; Muayad, M.; Mohammed, A.S.; Asteris, P.G. Analysis and Prediction of the Effect of Nanosilica on the Compressive Strength of Concrete with Different Mix Proportions and Specimen Sizes Using Various Numerical Approaches. *Struct. Concr.* **2023**, *24*, 4161–4184. [CrossRef]

85. Mirjalili, S. SCA: A Sine Cosine Algorithm for Solving Optimization Problems. *Knowl.-Based Syst.* **2016**, *96*, 120–133. [CrossRef]

86. Breiman, L. Random Forests. *Mach. Learn.* **2001**, *45*, 5–32. [CrossRef]

87. Sufian, M.; Ullah, S.; Ostrowski, K.A.; Ahmad, A.; Zia, A.; Sliwa-Wieczorek, K.; Siddiq, M.; Awan, A.A. An Experimental and Empirical Study on the Use of Waste Marble Powder in Construction Material. *Materials* **2021**, *14*, 3829. [CrossRef]

88. Bondar, D.; Nanukuttan, S.; Provis, J.L.; Soutsos, M. Efficient Mix Design of Alkali Activated Slag Concretes Based on Packing Fraction of Ingredients and Paste Thickness. *J. Clean. Prod.* **2019**, *218*, 438–449. [CrossRef]

89. Babaee, S.M. Corrosion of Reinforcement In Alkali-Activated Materials. Ph.D. Thesis, UNSW Sydney, Kensington, Australia, 2018.

90. Kar, A. Characterizations of Concretes with Alkali-Activated Binder and Correlating Their Properties from Micro- to Specimen Level. Ph.D. Thesis, West Virginia University, Morgantown, WV, USA, 2013.

91. Phoo-Ngernkham, T.; Phiangphimai, C.; Damrongwiriyanupap, N.; Hanjitsuwan, S.; Thumrongvut, J.; Chindaprasirt, P. A Mix Design Procedure for Alkali-Activated High-Calcium Fly Ash Concrete Cured at Ambient Temperature. *Adv. Mater. Sci. Eng.* **2018**, *2018*, 2460403. [CrossRef]

92. Madhuri, G.M.; Rao, K.S. Engineering Properties of Alkali Activated Slag Concrete Under Ambient And Heat Curing. *Int. J. Eng. Trends Technol.* **2017**, *50*, 161–166. [CrossRef]

93. Gu, L.; Visintin, P.; Bennett, T. Evaluation of Accelerated Degradation Test Methods for Cementitious Composites Subject to Sulfuric Acid Attack; Application to Conventional and Alkali-Activated Concretes. *Cem. Concr. Compos.* **2018**, *87*, 187–204. [CrossRef]

94. K, N.V.; Babu, D.L.V. Assessing the Performance of Molarity and Alkaline Activator Ratio on Engineering Properties of Self-Compacting Alkaline Activated Concrete at Ambient Temperature. *J. Build. Eng.* **2018**, *20*, 137–155. [CrossRef]

95. Shahrajabian, F.; Behfarnia, K. The Effects of Nano Particles on Freeze and Thaw Resistance of Alkali-Activated Slag Concrete. *Constr. Build. Mater.* **2018**, *176*, 172–178. [CrossRef]

96. Alzeebaree, R.; Çevik, A.; Nematollahi, B.; Sanjayan, J.; Mohammedameen, A.; Gülşan, M.E. Mechanical Properties and Durability of Unconfined and Confined Geopolymer Concrete with Fiber Reinforced Polymers Exposed to Sulfuric Acid. *Constr. Build. Mater.* **2019**, *215*, 1015–1032. [CrossRef]

97. Bhardwaj, B.; Kumar, P. Comparative Study of Geopolymer and Alkali Activated Slag Concrete Comprising Waste Foundry Sand. *Constr. Build. Mater.* **2019**, *209*, 555–565. [CrossRef]

98. Farhan, N.A.; Sheikh, M.N.; Hadi, M.N.S. Investigation of Engineering Properties of Normal and High Strength Fly Ash Based Geopolymer and Alkali-Activated Slag Concrete Compared to Ordinary Portland Cement Concrete. *Constr. Build. Mater.* **2019**, *196*, 26–42. [CrossRef]

99. Gopalakrishnan, R.; Chinnaraju, K. Durability of Ambient Cured Alumina Silicate Concrete Based on Slag/Fly Ash Blends against Sulfate Environment. *Constr. Build. Mater.* **2019**, *204*, 70–83. [CrossRef]

100. Deb, P.S.; Nath, P.; Sarker, P.K. The Effects of Ground Granulated Blast-Furnace Slag Blending with Fly Ash and Activator Content on the Workability and Strength Properties of Geopolymer Concrete Cured at Ambient Temperature. *Mater. Des.* **2014**, *62*, 32–39. [CrossRef]

101. Gülşan, M.E.; Alzeebaree, R.; Rasheed, A.A.; Niş, A.; Kurtoğlu, A.E. Development of Fly Ash/Slag Based Self-Compacting Geopolymer Concrete Using Nano-Silica and Steel Fiber. *Constr. Build. Mater.* **2019**, *211*, 271–283. [CrossRef]

102. Gunasekara, C.; Law, D.; Bhuiyan, S.; Setunge, S.; Ward, L. Chloride Induced Corrosion in Different Fly Ash Based Geopolymer Concretes. *Constr. Build. Mater.* **2019**, *200*, 502–513. [CrossRef]

103. Okoye, F.N.; Durgaprasad, J.; Singh, N.B. Mechanical Properties of Alkali Activated Flyash/Kaolin Based Geopolymer Concrete. *Constr. Build. Mater.* **2015**, *98*, 685–691. [CrossRef]

104. Shaikh, F.U.A. Mechanical and Durability Properties of Fly Ash Geopolymer Concrete Containing Recycled Coarse Aggregates. *Int. J. Sustain. Built Environ.* **2016**, *5*, 277–287. [CrossRef]

105. Gunasekara, C.; Law, D.W.; Setunge, S. Long Term Permeation Properties of Different Fly Ash Geopolymer Concretes. *Constr. Build. Mater.* **2016**, *124*, 352–362. [CrossRef]

106. Okoye, F.N.; Durgaprasad, J.; Singh, N.B. Fly Ash/Kaolin Based Geopolymer Green Concretes and Their Mechanical Properties. *Data Brief* **2015**, *5*, 739–744. [CrossRef] [PubMed]

107. Xie, T.; Ozbakkaloglu, T. Behavior of Low-Calcium Fly and Bottom Ash-Based Geopolymer Concrete Cured at Ambient Temperature. *Ceram. Int.* **2015**, *41*, 5945–5958. [CrossRef]

108. Ramagiri, K.K.; Chauhan, D.R.; Gupta, S.; Kar, A.; Adak, D.; Mukherjee, A. High-Temperature Performance of Ambient-Cured Alkali-Activated Binder Concrete. *Innov. Infrastruct. Solut.* **2021**, *6*, 71. [CrossRef]

109. Humad, A.M.; Kothari, A.; Provis, J.L.; Cwirzen, A. The Effect of Blast Furnace Slag/Fly Ash Ratio on Setting, Strength, and Shrinkage of Alkali-Activated Pastes and Concretes. *Front. Mater.* **2019**, *6*, 9. [CrossRef]

110. Farhan, N.A.; Sheikh, M.N.; Hadi, M.N.S. Engineering Properties of Ambient Cured Alkali-Activated Fly Ash–Slag Concrete Reinforced with Different Types of Steel Fiber. *J. Mater. Civ. Eng.* **2018**, *30*, 04018142. [CrossRef]

111. Valencia Saavedra, W.G.; Angulo, D.E.; Mejía de Gutiérrez, R. Fly Ash Slag Geopolymer Concrete: Resistance to Sodium and Magnesium Sulfate Attack. *J. Mater. Civ. Eng.* **2016**, *28*, 04016148. [CrossRef]

112. Orosz, K.; Humad, A.; Hedlund, H.; Cwirzen, A. Autogenous Deformation of Alkali-Activated Blast Furnace Slag Concrete Subjected to Variable Curing Temperatures. *Adv. Civ. Eng.* **2019**, *2019*, 6903725. [CrossRef]

113. Aslani, F.; Asif, Z. Properties of Ambient-Cured Normal and Heavyweight Geopolymer Concrete Exposed to High Temperatures. *Materials* **2019**, *12*, 740. [CrossRef] [PubMed]

114. Sathanandam, T.; Awoyera, P.O.; Vijayan, V.; Sathishkumar, K. Low Carbon Building: Experimental Insight on the Use of Fly Ash and Glass Fibre for Making Geopolymer Concrete. *Sustain. Environ. Res.* **2017**, *27*, 146–153. [CrossRef]

115. Puertas, F.; González-Fonteboa, B.; González-Taboada, I.; Alonso, M.M.; Torres-Carrasco, M.; Rojo, G.; Martínez-Abella, F. Alkali-Activated Slag Concrete: Fresh and Hardened Behaviour. *Cem. Concr. Compos.* **2018**, *85*, 22–31. [CrossRef]

116. Aliabdo, A.A.; Abd Elmoaty, A.E.M.; Emam, M.A. Factors Affecting the Mechanical Properties of Alkali Activated Ground Granulated Blast Furnace Slag Concrete. *Constr. Build. Mater.* **2019**, *197*, 339–355. [CrossRef]

117. Thunuguntla, C.S.; Gunneswara Rao, T.D. Mix Design Procedure for Alkali-Activated Slag Concrete Using Particle Packing Theory. *J. Mater. Civ. Eng.* **2018**, *30*, 04018113. [CrossRef]

118. Wardhono, A. The Durability of Fly Ash Geopolymer and Alkali-Activated Slag Concretes. Ph.D. Thesis, RMIT University, Melbourne, Australia, 2015.

119. Wardhono, A.; Law, D.W.; Sutikno; Dani, H. The Effect of Slag Addition on Strength Development of Class C Fly Ash Geopolymer Concrete at Normal Temperature. *AIP Conf. Proc.* **2017**, *1887*, 020030.

120. Mithun, B.M.; Narasimhan, M.C. SELF-Cured Alkali Activated Slag Concrete Mixes-an Experimental Study. *Int. J. Civ. Environ. Eng.* **2014**, *8*, 477–482.

121. Pilehvar, S.; Cao, V.D.; Szczotok, A.M.; Carmona, M.; Valentini, L.; Lanzón, M.; Pamies, R.; Kjøniksen, A.-L. Physical and Mechanical Properties of Fly Ash and Slag Geopolymer Concrete Containing Different Types of Micro-Encapsulated Phase Change Materials. *Constr. Build. Mater.* **2018**, *173*, 28–39. [CrossRef]

122. Fang, G.; Ho, W.K.; Tu, W.; Zhang, M. Workability and Mechanical Properties of Alkali-Activated Fly Ash-Slag Concrete Cured at Ambient Temperature. *Constr. Build. Mater.* **2018**, *172*, 476–487. [CrossRef]

123. Reddy, M.S.; Dinakar, P.; Rao, B.H. Mix Design Development of Fly Ash and Ground Granulated Blast Furnace Slag Based Geopolymer Concrete. *J. Build. Eng.* **2018**, *20*, 712–722. [CrossRef]

124. Rafeet, A.; Vinai, R.; Soutsos, M.; Sha, W. Guidelines for Mix Proportioning of Fly Ash/GGBS Based Alkali Activated Concretes. *Constr. Build. Mater.* **2017**, *147*, 130–142. [CrossRef]

125. Lee, N.K.; Lee, H.K. Setting and Mechanical Properties of Alkali-Activated Fly Ash/Slag Concrete Manufactured at Room Temperature. *Constr. Build. Mater.* **2013**, *47*, 1201–1209. [CrossRef]

126. Nath, P.; Sarker, P.K. Effect of GGBFS on Setting, Workability and Early Strength Properties of Fly Ash Geopolymer Concrete Cured in Ambient Condition. *Constr. Build. Mater.* **2014**, *66*, 163–171. [CrossRef]

127. Hosseini, S.; Mousavi, A.; Monjezi, M. Prediction of Blast-Induced Dust Emissions in Surface Mines Using Integration of Dimensional Analysis and Multivariate Regression Analysis. *Arab. J. Geosci.* **2022**, *15*, 163. [CrossRef]

128. Kahraman, E.; Hosseini, S.; Taiwo, B.O.; Fissha, Y.; Jebutu, V.A.; Akinlabi, A.A.; Adachi, T. Fostering Sustainable Mining Practices in Rock Blasting: Assessment of Blast Toe Volume Prediction Using Comparative Analysis of Hybrid Ensemble Machine Learning Techniques. *J. Saf. Sustain.* **2024**, *1*, 75–88. [CrossRef]

129. Taiwo, B.O.; Hosseini, S.; Fissha, Y.; Kilic, K.; Olusola, O.A.; Chandrahas, N.S.; Li, E.; Akinlabi, A.A.; Khan, N.M. Indirect Evaluation of the Influence of Rock Boulders in Blasting to the Geohazard: Unearthing Geologic Insights Fused with Tree Seed Based LSTM Algorithm. *Geohazard Mech.* 2024; *in press*.
130. Hosseini, S.; Mousavi, A.; Monjezi, M.; Khandelwal, M. Mine-to-Crusher Policy: Planning of Mine Blasting Patterns for Environmentally Friendly and Optimum Fragmentation Using Monte Carlo Simulation-Based Multi-Objective Grey Wolf Optimization Approach. *Resour. Policy* **2022**, *79*, 103087. [CrossRef]
131. Wei, W.; Li, X.; Liu, J.; Zhou, Y.; Li, L.; Zhou, J. Performance Evaluation of Hybrid Woa-svr and Hho-svr Models with Various Kernels to Predict Factor of Safety for Circular Failure Slope. *Appl. Sci.* **2021**, *11*, 1922. [CrossRef]
132. Nguyen, H.; Drebenstedt, C.; Bui, X.-N.; Bui, D.T. Prediction of Blast-Induced Ground Vibration in an Open-Pit Mine by a Novel Hybrid Model Based on Clustering and Artificial Neural Network. *Nat. Resour. Res.* **2020**, *29*, 691–709. [CrossRef]
133. Zhou, J.; Su, Z.; Hosseini, S.; Tian, Q.; Lu, Y.; Luo, H.; Xu, X.; Chen, C.; Huang, J. Decision Tree Models for the Estimation of Geo-Polymer Concrete Compressive Strength. *Math. Biosci. Eng.* **2024**, *21*, 1413–1444. [CrossRef]
134. Taylor, K.E. Summarizing Multiple Aspects of Model Performance in a Single Diagram. *J. Geophys. Res. Atmos.* **2001**, *106*, 7183–7192. [CrossRef]
135. Zhang, H.; Zhou, J.; Armaghani, D.J.; Tahir, M.M.; Pham, B.T.; Huynh, V. Van A Combination of Feature Selection and Random Forest Techniques to Solve a Problem Related to Blast-Induced Ground Vibration. *Appl. Sci.* **2020**, *10*, 869. [CrossRef]
136. Zhao, J.; Hosseini, S.; Chen, Q.; Armaghani, D.J. Super Learner Ensemble Model: A Novel Approach for Predicting Monthly Copper Price in Future. *Resour. Policy* **2023**, *85*, 103903. [CrossRef]